The MeerKAT 1.3 GHz Survey of the Small Magellanic Cloud

W. D. Cotton,[1,2⋆] M. D. Filipović,[3] F. Camilo,[2] R. Indebetouw,[4,1] R. Z. E. Alsaberi,[3] J. O. Anih,[5] M. Baker,[5] T. S. Bastian,[1] I. Bojičić,[3] E. Carli,[6] F. Cavallaro,[7] E. J. Crawford,[3] S. Dai,[3,8] F. Haberl,[9] L. Levin,[6] K. Luken,[3] C. M. Pennock,[10] N. Rajabpour,[3] B. W. Stappers,[6] J. Th. van Loon,[5] A. A. Zijlstra,[11] S. Buchner,[2] M. Geyer,[2,12] S. Goedhart,[2] M. Serylak[2,13,14]

[1]*National Radio Astronomy Observatory, 520 Edgemont Road, Charlottesville, VA 22903, USA*
[2]*South African Radio Astronomy Observatory (SARAO), 2 Fir Street, Black River Park, Observatory, Cape Town 7925, South Africa*
[3]*Western Sydney University, Locked Bag 1797, Penrith South DC, NSW 2751, Australia*
[4]*Department of Astronomy, University of Virginia, Charlottesville, VA 22904, USA*
[5]*Lennard-Jones Laboratories, Keele University, Staffordshire ST5 5BG, UK*
[6]*Jodrell Bank Centre for Astrophysics, Department of Physics and Astronomy, The University of Manchester, Manchester M13 9PL, UK*
[7]*INAF-Osservatorio Astrofisico di Catania, Via S. Sofia 78, I-95123 Catania, Italy*
[8]*CSIRO Astronomy and Space Science, PO Box 76, Epping, NSW 1710, Australia*
[9]*Max-Planck-Institut für extraterrestrische Physik, Gießenbachstraße 1, D-85748 Garching, Germany*
[10]*Institute for Astronomy, University of Edinburgh, Royal Observatory, Blackford Hill, Edinburgh EH9 3HJ, UK*
[11]*Jodrell Bank Centre for Astrophysics, The University of Manchester, Oxford Road M13 9PL, UK*
[12]*High Energy Physics, Cosmology & Astrophysics Theory (HEPCAT) Group, Department of Mathematics & Applied Mathematics, University of Cape Town, Cape Town 7700, South Africa*
[13]*SKA Observatory, Jodrell Bank, Lower Withington, Macclesfield, SK11 9FT, UK*
[14]*Department of Physics and Astronomy, University of the Western Cape, Bellville, Cape Town, 7535, South Africa*

Accepted 19 Jan. 2024. Received 15 Jan 2024; in original form 13 Nov 2023

ABSTRACT

We present new radio continuum images and a source catalogue from the MeerKAT survey in the direction of the Small Magellanic Cloud (SMC). The observations, at a central frequency of 1.3 GHz across a bandwidth of 0.8 GHz, encompass a field of view ∼7°×7° and result in images with resolution of 8 arcsec. The median broad-band Stokes I image Root Mean Squared noise value is ∼11 μJy beam^{-1}. The catalogue produced from these images contains 108,330 point sources and 517 compact extended sources. We also describe a UHF (544–1088 MHz) single pointing observation. We report the detection of a new confirmed Supernova Remnant (SNR) (MCSNR J0100–7211) with an X-ray magnetar at its centre and 10 new SNR candidates. This is in addition to the detection of 21 previously confirmed SNRs and two previously noted SNR candidates. Our new SNR candidates have typical surface brightness an order of magnitude below those previously known, and on the whole they are larger. The high sensitivity of the MeerKAT survey also enabled us to detect the bright end of the SMC Planetary Nebulae (PNe) sample – point-like radio emission is associated with 38 of 102 optically known PNe, of which 19 are new detections. Lastly, we present the detection of three foreground radio stars amidst 11 circularly polarised sources, and a few examples of morphologically interesting background radio galaxies from which the radio ring galaxy ESO 029–G034 may represent a new type of radio object.

Key words: Magellanic Clouds – radio continuum – catalogues – SNRs – AGNs – PNe

1 INTRODUCTION

Over the past 50 years, several radio surveys have greatly improved our knowledge of the neighbouring SMC galaxy and its source populations. This is an exciting time for the study of nearby galaxies,

⋆ E-mail: bcotton@nrao.edu

especially in radio wavebands using the new generation of radio telescopes such as MeerKAT, the Australian Square Kilometre Array Pathfinder (ASKAP) and the Murchison Widefield Array (MWA). These nearby Local Group galaxies offer ideal laboratories since they are close enough to be resolved, yet located at well-known distances (see e.g. Pietrzyński et al. 2019).

New generations of Magellanic Cloud (MC) surveys across the entire electromagnetic spectrum provide a major opportunity to study different objects and processes in the evolution and elemental enrichment of the Interstellar Medium (ISM). The study of these in different domains, including radio, IR, optical and X-ray (Sturm et al. 2013b), allow a better understanding of objects such as SNRs, PNe, young stellar objects (YSOs), H II regions and (super)bubbles and their environments. Also, the SMC's large-scale properties such as its magnetic field are essential to understand the kinematics and dynamics of this galaxy.

The focus of our new radio continuum study – the SMC – is a gas-rich irregular and nearby dwarf galaxy interacting with the Large Magellanic Cloud (LMC) and Milky Way (MW) halo. The nearby distance of 62.44±0.47 kpc[1] but with the sizeable line-of-sight depth reaching 7 kpc (Graczyk et al. 2020) and the low Galactic foreground emission and absorption ($N_{\rm HI} \sim 6{\times}10^{20}$ cm^{-2}) enables the entire source population in the SMC to be studied in various wavebands and at excellent spatial resolution. The SMC also attracts particular attention because it has 5 times lower metallicity in its ISM than the solar neighbourhood. At the same time, a vast amount of foreground and especially background sources pose for detailed investigation.

For these reasons, the SMC has been the target of many radio studies over the past 50 years. Starting in the 1970s, the SMC has been surveyed by single-dish and interferometric radio telescopes. These large-scale observational campaigns have produced several catalogues of sources towards the SMC (Clarke 1976; McGee et al. 1976; Haynes et al. 1986; Wright & Otrupcek 1990; Filipović et al. 1997; Turtle et al. 1998; Filipović et al. 1998; Filipović et al. 2002; Payne et al. 2004; Filipović et al. 2005; Reid et al. 2006; Payne et al. 2007; Wong et al. 2011a; Crawford et al. 2011; Wong et al. 2011b, 2012a,b; For et al. 2018; Joseph et al. 2019).

The MeerKAT survey of the SMC field presented here is a significant improvement on previous similar radio continuum studies. MeerKAT's high resolution and sensitivity have already been demonstrated in other studies (e.g., Heywood et al. 2022). In this paper, we present point and compact extended source catalogues from the MeerKAT SMC survey. These catalogues were obtained from images taken at the broad band of 1283.8 MHz (λ = 23 cm; L-band) and 12 sub-bands. We also present results on several new objects found in these images.

The paper is organised as follows: Section 2 describes the MeerKAT observations, reduction, and data used to create the source lists, with data release details in Section 2.7. In Section 3.1 we describe the source detection methods used and Section 3.2 describes the new MeerKAT source catalogues including spectral indices (Section 3.3), while in Section 3.4 we compare our work to previous catalogues of point sources towards the SMC. In Section 4 we present some of the early science results from this survey which includes the study of SNRs (Sections 4.1, 4.2), pulsars (Section 4.3), and PNe (Section 4.4), radio stars (Section 4.5), while in Section 4.6, we briefly discuss other sources of interest, including those behind the SMC. The bulk of the discussion concerns the L-band mosaics.

[1] For easier comparison with previous studies, we adopt a distance of 60 kpc for all our calculations in this paper as most of the previous studies used this value.

2 DATA

2.1 Observations

2.1.1 L-band

Observations of the SMC were made with the MeerKAT array primarily at L-band (856 to 1712 MHz) using 8-second integrations and 4096 spectral channels across the band. All four combinations of the linearly polarised feeds were recorded. The MeerKAT array is described in more detail in Jonas (2016); Camilo et al. (2018); Mauch et al. (2020). These observations used project code SSV-20190715-FC-02.

Since the SMC is substantially larger than the field of view of the MeerKAT antennas, the observations consisted of a mosaic of pointings on a hexagonal pattern with an offset between centres of 29.6 arcmin which gives relatively uniform sensitivity. The mosaic was initially covered in seven sessions of eight or nine pointings each, cycling among 5 min scans on the pointings for roughly 10 hours in each session. This gives approximately 1 hour of integration on each pointing but is composed of many snapshots spread widely in hour angle to improve *uv* coverage. The centre of the mosaic is at RA(J2000)=01:00:00.0, Dec(J2000)=–73:00:00. A total of 60 individual pointing centres were observed across the field of 7.08°×7.08°.

PKS B1934−638 and PKS 0408−65 were used for the delay, band-pass and flux density calibration; J0252–7104 was the gain (astrometric) calibrator and 3C138 was the polarised calibrator. PKS B1934−638, PKS 0408−65, and 3C138 were observed for 10 min every few hours as available and J0252–7104 was observed for 2 minutes every half hour. The flux density scale is set to the spectrum of PKS B1934−638 given in Reynolds (1994):

$$\log(S) = -30.7667 + 26.4908(\log\nu) - 7.0977(\log\nu)^2 + 0.605334(\log\nu)^3\,, \quad (1)$$

where S is the flux density in Jy and ν is the frequency in MHz.

The observations were obtained between 21 July 2019 and 29 September 2019 and are summarised in Table 1 where times include calibration overheads. Two of the sessions were divided into multiple blocks which were calibrated individually. After an initial imaging, several of the pointings had undiagnosed imaging artifacts and these pointings were reobserved. Furthermore, several pointings were dynamic range limited and additional observations were made. Later reduction managed to recover the bulk of the affected pointings' data which was then incorporated into the final imaging. The additional observations had the net effect of improving the dynamic range in the parts of the mosaic with large-scale, bright emission.

2.1.2 UHF

A single pointing observation of the SMC was also made in the UHF band (544–1088 MHz) on 6 and 7 Feb 2020. There were 13.5 hours of observations, including calibration, and 10.3 hours on the SMC. The pointing centre was RA(J2000)=00:52:44.0 and Dec(J2000)=–72:49:42. Fifty three of the 64 antennas were in the array on 6 Feb and 59 on 7 Feb. Data were recorded with 8-second

Table 1. MeerKAT L-band observations of the SMC.

Date	Total Time (hours)	Note
21 Jul 2019	10.9	Session 1
24 Jul 2019	10.5	Session 2
31 Jul 2019	9.7	Session 3
04 Aug 2019	10.3	Session 4
06 Aug 2019	5.3	Session 5
06 Aug 2019	6.0	Session 5
11 Aug 2019	3.2	Session 6
12 Aug 2019	5.5	Session 6
13 Aug 2019	6.7	Session 6
13 Aug 2019	8.9	Session 7
11 Sep 2019	4.5	Reobserve
12 Sep 2019	12.2	Reobserve
29 Sep 2019	12.1	Reobserve

sampling, 4096 spectral channels and all four correlation products. These observations are under project code SSV-20200131-SP-01.

2.2 Calibration

Initial calibration and data editing were as described in Mauch et al. (2020) and Cotton et al. (2020), and we used the OBIT package described by Cotton (2008)[2]. This processing trims the edge channels and divides the remainder into 8 'spectral windows' for calibration purposes. A standard list of channels always affected by strong Radio-Frequency Interference (RFI) was flagged. Calibration and editing steps are interleaved.

The polarisation calibration was based on the hardware 'noise diode' calibration performed at the beginning of each observing session. This involves injecting a signal into each feed which allows for measuring the phase and delay differences between the orthogonal feeds after the injection point. Residual differences were estimated from the polarised calibrator and the instrumental polarisation (a.k.a. 'leakage') was estimated from PKS B1934−638 and PKS 0408−65 (assumed unpolarised) and J0252−7104. This method is described in more detail in Cotton et al. (2020).

2.3 Imaging

The L-band data were imaged in Stokes I, Q, U and V using the OBIT task MFIMAGE which is described more fully in Cotton et al. (2018). UHF data were imaged only in Stokes I. This imaging program uses multiple constant fractional bandwidth frequency sub-bands which are imaged independently and CLEANed jointly to accommodate the frequency dependence of the sky and the antenna gain pattern. Faceting (Perley 1999) is used to correct for the non-coplanarity of the array. This allows for fully covering a given field of view while including outlying facets around stronger sources.

Imaging used 5 per cent fractional bandwidth sub-bands, fully imaged at L-band to a radius of 1.2 degrees with outlying facets to 1.5 degrees centred on sources estimated from the 843 MHz Sydney University Molonglo Sky Survey (SUMSS) catalogue (Mauch et al. 2003) to appear brighter than 1 mJy. At ultra high frequency (UHF) the field of view had a radius of 2.5 degrees and used outliers to 3 degrees. All pointings were subjected to two-phase self-calibrations and also amplitude and phase self-calibration if the peak brightness in the image exceeded 0.7 Jy beam^{-1}. A Briggs Robust factor of –1.5 (AIPS/OBIT usage where the scale goes from –5 (pure uniform) to 5 (natural) weights) was used to result in a typical resolution of 7.5 arcsec at L-band. At UHF the restoring beam is 13.3 × 11.0 arcsec^2. CLEANing used a gain of 0.05 and proceeded to a maximum of 125 000 components or a residual of 60 μJy beam^{-1} in Stokes I, 10 000 components or a residual of 40 μJy beam^{-1} in Stokes Q and U and 500 components or a residual of 20 μJy beam^{-1} in Stokes V.

The procedure described above makes only direction-independent gain corrections and is insufficient to produce noise-limited images in pointings with bright and extended emission. For a number of cases, 'peeling' (Noordam 2004; Smirnov & Tasse 2015) was applied to allow direction-dependent gain correction for the brighter sources in the field of a given pointing. In a few cases, a multiresolution CLEAN was also used to better image large-scale emission. For these, the second resolution of approximately 30 arcsec Full Width at Half-Maximum (FWHM) was used.

2.4 Astrometric corrections

A number of systematic astrometric errors affecting MeerKAT images are discussed in Knowles et al. (2022); the most important of these for the SMC images is thought to be the low-accuracy geometric model used in the correlator. The pointing images had residual astrometric variations on the sub-arcsecond level. These errors were estimated by comparing the positions of compact radio sources as extracted by AEGEAN (Section 3) to quasar positions from MilliQuas[3] (Flesch 2021). Sources were selected from the MeerKAT source catalogue with a ratio of integrated vs peak flux density <1.3, and measured uncertainties less than 2 arcsec in RA and Dec, i.e. compact and point sources with good positional precision.

MilliQuas sources in the imaged region were retrieved from the HEASARC interface to version 7.4 of the catalogue (Flesch 2021, Dec 2021), and matched to the nearest MeerKAT catalogue source within 2 arcsec. Of the 1489 MilliQuas sources, 745 are matched to MeerKAT sources. There was a clear systematic offset of 0.193±0.031 arcsec in RA and –0.734±0.020 arcsec in Dec; this correction was applied (added) to all L-band pointings. After removing that global mean offset, matched sources within 0.4 degrees of each pointing centre were considered. A pointing was determined to have a significant measurable residual offset if it had: at least five matched sources, a residual offset (after removing the full-mosaic offset) of more than 0.15 arcsec and a residual offset of greater than the dispersion of individual source offsets for that field. The fields with sufficiently significant offsets to be applied were corrected and are listed in Table 2. Based on the remaining dispersion in individual source offsets after these per-field corrections, we estimate that the astrometric uncertainty of a typical source in the mosaic is better than 0.25 arcsec. Additional comparisons with other catalogues are given in Section 3.4.1.

2.5 Mosaicing

Individual L-band pointing images in Stokes I, Q, U and V were combined into single mosaics covering the SMC using a process

[2] http://www.cv.nrao.edu/~bcotton/Obit.html

[3] `https://heasarc.gsfc.nasa.gov/W3Browse/all/milliquas.html`

Table 2. Pointings with individual astrometric corrections applied. Note that the pointings were arranged in a hexagonal pattern in a set of rows ('R') and columns ('C').

Name	Centre RA	Centre Dec	RA offset (arcsec)	Dec offset (arcsec)
SMC1R01C09	00:32:08.52	–73:59:15.5	–0.078	+0.216
SMC1R01C11	00:32:08.52	–74:58:31.1	–0.110	–0.239
SMC1R03C09	00:46:09.36	–73:59:15.6	–0.185	–0.266
SMC1R03C11	00:46:09.36	–74:58:31.1	+0.130	–0.250
SMC1R06C02	01:06:05.37	–70:31:51.1	–0.653	+0.471
SMC1R06C04	01:06:05.37	–71:31:06.7	–0.309	–0.050
SMC1R06C06	01:06:05.37	–72:30:22.2	+0.353	+0.047
SMC1R07C01	01:13:00.74	–70:02:13.3	+0.476	+0.336
SMC1R07C03	01:13:00.74	–71:01:28.9	+0.108	–0.370
SMC1R10C04	01:33:06.86	–71:31:06.7	+0.318	–0.199

similar to that described in Brunthaler et al. (2021). The optimal sensitivity combination used

$$M(x,y) = \frac{\sum_{i=1}^{n} P_i(x,y) I'_i(x,y)}{\sum_{i=1}^{n} P_i^2(x,y)}, \quad (2)$$

where $M(x,y)$ is the combined image as a function of sky coordinates, n is the number of pointing images contributing to the mosaic, P_i is the antenna power gain pattern for pointing i and I' is the pointing image interpolated to the grid of the mosaic. This procedure will correct the mosaic image for variations in the antenna power gain across the field of view. Prior to the combination, the pointing images were convolved to a resolution of 8 arcsec and the coordinates were corrected as described in Section 2.4.

The sub-band mosaics were formed using Eq. 2 and used to derive a total flux density and spectral index (defined by $S \propto \nu^{\alpha}$, where S is flux density, ν is frequency and α is the spectral index) as described in Section 2.7. The off-source Root Mean Squared (rms) in quieter portions of the Stokes I image is 11 μJy beam^{-1}, 7.1 μJy beam^{-1} for Stokes Q, 7.6 μJy beam^{-1} for Stokes U and 7.9 μJy beam^{-1} for Stokes V. In Fig. 1 we show the central part of the Stokes I image.

2.6 UHF

Since the UHF data were in a single pointing, the data were primary beam corrected rather than formed into a mosaic. The broadband image was constructed from a weighted average of the subband planes using weighting proportional to the inverse of the plane RMS. This results in an effective frequency at the pointing center of 870.0 MHz. The RMS in the image uncorrected for the primary beam is 8.6 μJy beam^{-1}.

As the gain of the antennas away from the pointing center varies with frequency, the effective frequency declines with distance from the pointing center. A frequency dependent correction to the subband pixel values following the technique of Cotton et al. 2024 (submitted) using an assumed spectral index of α=-0.6 was used to adjust all parts of the image to the same effective reference frequency.

2.7 Data products

There are a number of data products being made available with this paper from the observations of the SMC.

- **Visibility data:** Raw L-band visibility data is available from the South African Radio Astronomy Observatory (SARAO) archive (`https://archive.sarao.ac.za/`) under project code SSV-20190715-FC-02. The UHF data is under project code SSV-20200131-SP-01. Catalogues and images are available from DOI `https://doi.org/10.48479/1fdb-r233`.
- **L-band mosaic images:** The mosaic FITS images are as described in Cotton (2019). The mosaics in Stokes I, Q, U and V are 7.08° × 7.08° with 1.5 arcsec pixels centred at J2000 position RA=01:00:0.0 and Dec=–73:00:00.0. The mosaic cubes contain 16 planes. The broad-band flux densities are averages, weighted by Stokes I plane RMS^{-1}, giving a reference frequency of 1310.89 MHz. More details of the derivation of the reference frequency is given in Cotton et al.2024 (submitted). For each pixel in the Stokes I mosaic with an adequate signal-to-noise ratio and an average Stokes I intensity in excess of 250 μJy beam^{-1}, a least squares fit was performed to derive the spectral index. Other pixels are blanked. The first plane is the band average flux density, the second plane is the spectral index, and subsequent planes are the frequency bins centred at the frequencies given in Table 3. Two planes are totally blanked due to RFI. Stokes Q, U and V images have a second plane which is blanked. This plane is nominally the spectral index but since Q and U are also subjected to Faraday rotation, this is not meaningful. A second total intensity image containing the band average flux density, spectral index and least squares fitting error estimates is also provided.
- **UHF image:** The primary beam and effective frequency corrected Stokes I is given in two forms similar to the L-band mosaics. The minimum Stokes I for fitting spectral index was 50 μJy beam^{-1}. The effective reference frequency is 870.0 MHz. These files are SMC_UHF_I_Cube.fits.gz and SMC_UHF_I_Fit.fits.gz.
- **Catalogues:** The catalogues underlying this article are available on the CDS/VizieR (`https://cds.u-strasbg.fr/`). The full point and compact extended source catalogues (Tables 4 and 5) are also provided through the CDS/VizieR service. DS9 region files for the Bright Compact Extended sample of sources are also provided (Section 3.2).

2.8 Data limitations

There are a number of limitations of the MeerKAT observations that can affect the scientific interpretation of the results. Some of these have been mitigated in the data products distributed but will remain in the raw visibility data. These limitations are similar to those discussed in Knowles et al. (2022) although more have been corrected in the SMC data products.

2.8.1 Dynamic range

While the excellent *uv* coverage of MeerKAT generally gives a good dynamic range, Direction Dependent Effects (DDEs) can result in significant artifacts due to bright sources. This is especially true if there are multiple bright, widely separated sources that are not adequately corrected by direction-independent self-calibration. The expected DDEs include pointing errors, variable ionospheric refraction and asymmetries in the array antenna patterns. DDEs are explored in detail in Smirnov (2011).

As described in Section 2.3, the pointing fields most affected by dynamic range limiting DDEs have had 'peeling' applied to reduce the Stokes I artifacts due to the strongest sources. These improved pointing images were then incorporated into the mosaic data products. The raw visibility data still includes these effects.

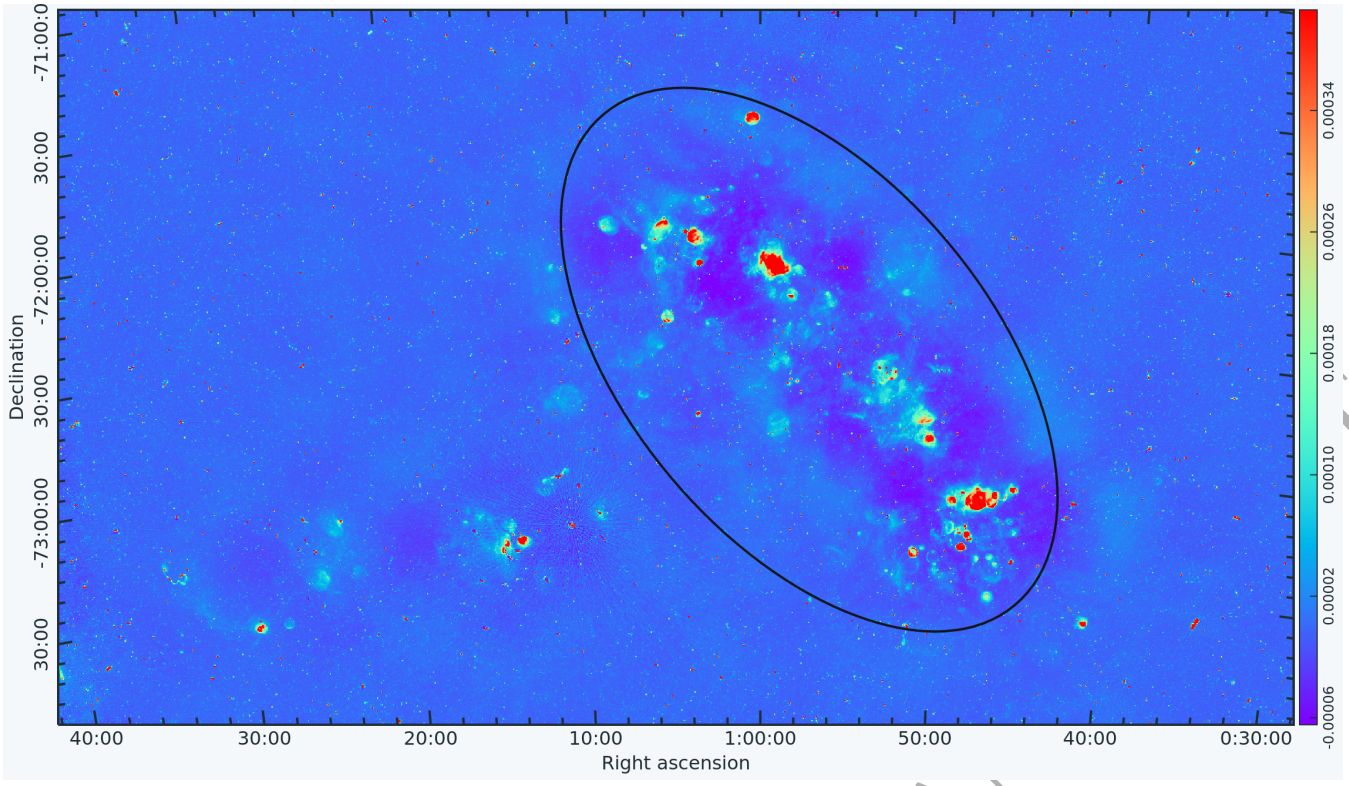

Figure 1. MeerKAT broad band Stokes I image of the central portion of the SMC field. The black ellipse indicates an area of the so-called SMC bar region. The colour bar (linear scale) on the right-hand side is in units of Jy beam^{-1}.

2.8.2 *Largest angular size*

The largest structure that can be imaged using interferometer data is determined by the *uv* coverage of the shortest spacings. As the *uv* location of a given measurement depends on the observing frequency, the factor of two between the highest and lowest frequencies in MeerKAT L-band observations results in a factor of two difference in the largest structure that can be imaged at the top and bottom of the band. This effect can result in a severe spurious steepening of the apparent spectrum for regions that are increasingly resolved out with increasing frequency. For a 1 Jy 10 arcmin FWHM Gaussian source, the visibility on typical short baselines is 0.32 at the bottom of the band and 0.02 at the top. This effect can severely limit the maximum flux density that can be recovered. Sources significantly smaller than 10 arcmin should not be seriously affected but larger ones can be.

A further complication of the limited short baseline coverage is the 'missing zero spacing' problem. If the deconvolution of a bright, extended feature does not recover all of the flux density, the feature will be surrounded by a negative 'bowl'. This bowl will be frequency dependent, more pronounced at higher frequencies, and complicates the estimation of flux density and especially spectral index. These bowls can be easily seen in Fig. 1.

2.8.3 *Flux density and spectral index*

The wide fractional bandpass of the MeerKAT L-band data allows the estimation of a wideband flux density and spectral index in pixels with adequate signal-to-noise. The result of the imaging process is a cube of images in 14 frequency bins (2 of which are totally blanked because of RFI). A simple weighted average of these will produce a brightness image whose reference frequency depends on the weighting, derived from the RMS^{-1} of fluctuations in spectral regions not affected by RFI. For pixels in which there is an adequate signal, a least squares fit can produce a spectral index at the reference frequency derived from the weighting. The spectral index image is the fitted value where available, else blanked. The SMC field contains emissions with a wide range of spectral indices, from ~1.0 to –1.5 or less.

The effective array antenna pattern is also not well known; variable pointing errors cause it to be broader than that of a single antenna. Errors in the assumed pattern (that of an individual antenna) cause the derived spectral index to appear more negative than it actually is with increasing distance from the pointing centre. The 'primary beam correction' is applied in the mosaic formation (Section 2.5) which reduces its errors in the mosaic products. This problem remains in the visibility data and in the UHF image.

2.8.4 *Astrometry*

The low-precision model used in the interferometer delay calculation can result in systematic position offsets in individual pointing images. These have been measured and corrected in the mosaic and catalogue data products as described in Section 2.4 but are uncorrected in the visibility data.

2.8.5 *Polarisation*

The images in the first plane of the Stokes Q, U and V cubes are meant to be suggestive of where there is polarised emission but should not be used for scientific interpretation. This plane is the

Table 3. Number of sources in each sub-band. The bandwidth of channel-0 is 811.455 MHz while other channels have ~5 per cent (~40-70 MHz) fractional bandwidth. Channels 8 and 9 are not used because of RFI. Compared to other channels, we note a dip in the number of matched sources in channels 3 and 14, likely due to localised RFI.

Channel	Frequency (MHz)	Total matched
0	1283	108,330
2	908.037	30,322
3	952.342	18,298
4	996.646	33,782
5	1043.46	34,929
6	1092.78	32,587
7	1144.61	23,872
10	1317.23	29,337
11	1381.18	34,415
12	1448.05	33,516
13	1519.94	21,346
14	1593.92	9,880
15	1656.2	18,032

band average of the Stokes Q, U and V frequency channel images and for Q and U is only meaningful in the unlikely case that the rotation measure, depolarisation and polarised spectral index are all zero. The band average linearly polarised intensity is reduced by a factor of ≥ 2 when |RM| exceeds about 25 rad m^{-2}.

Uncorrected instrumental polarisation is high towards the top end of the bandpass and away from the pointing centre (de Villiers & Cotton 2022). This effect is reduced in the mosaic and catalogue products but is uncorrected in the visibility data. Residual uncorrected instrumental polarisation limits the polarisation dynamic range near sources bright in total intensity.

3 MEERKAT SMC SOURCE CATALOGUES

3.1 Source detection

In a similar way to Filipović et al. (2021) and Pennock et al. (2021), we used Aegean, a compact source detection and flux extraction algorithm (Hancock et al. 2018), to create point source catalogues from the broad-band image (channel 0) and 12 sub-band images as listed in Table 3.

3.1.1 L-band Broad-band image

The broad-band (channel 0) results are derived from the weighted average Stokes I image with an effective frequency 1311 MHz rather than the band centre 1284 MHz.

We created the initial rms and background map in the channel 0 using the Background and Noise Estimation tool (BANE; part of the Aegean suite), and the initial point source catalogue by applying a simple blind search with default parameters for both BANE and Aegean. This initial search yielded >122 000 sources relatively evenly distributed across the field with a noticeable difference in the source density distribution in the central bar region structure (because of confusion and extended emission) and at the edge of the mosaic. The produced rms image was visually inspected and, as expected, because of the primary beam attenuation, the rms noise shows a rapid rise at the edge of the mosaic and consequently a fall-off in sensitivity.

In Fig. 2 we show the plot of local rms values vs. peak flux density of the associated sources from the initial catalogue. As can be seen, the distribution appears smooth except for a visible density excess in the region with rms >25 μJy beam^{-1} (vertical blue dashed line). We visually inspected about 10 per cent of sources from this excess. We noticed that all sources in the excess are located close to the edge of the mosaic (i.e. no sources are located in the high rms region of the central bar) and that more than 50 per cent of these sources appear to be false detections. Also, we noted a set of detections below the applied detection limit (S/N=5; red dash-dot line in Fig. 2). These detections are relatively evenly distributed across the image mosaic. After visual inspection, we found that similar to the excess set, it consists of many false positive detections.

In the case of bright compact extended sources (BCE; sources with angular sizes larger than resolving beam > ×1.5 beam size or from ~10 arcsec to 7.5 arcminutes; Fig. 3; e.g. resolved background sources, blended objects), the Aegean algorithm will attempt to fit multiple Gaussian components to the detected 'island' of emission (for more details see the Hancock et al. (2018) or Aegean documentation[4]). This poses a concern that the complex emission regions would get broken into multiple sources which would create a problem when comparing flux densities from this new catalogue to values from previous or future lower-resolution catalogues. Another issue we noticed by visual inspection is that a significant number of faint point sources in the vicinity of BCE sources have not been picked up by the Aegean algorithm (i.e. false negative detections). The most likely reason is that the averaged rms noise, close to the bright and complex emission, is significantly higher than the real noise measured outside these complex regions, and therefore the real but faint sources fail to reach the S/N ratio needed for detection. We visually assessed such deconvolution errors and determined that the deconvolution is sufficiently good that the fainter sources near bright ones are real and we kept them in the catalogue.

To resolve the above-identified issues, we produced the final catalogue (see Table 4) using the following steps:

(i) Using the initial rms map we produced a masked channel 0 image where the region with averaged rms>25 μJy beam^{-1} and at the edge of the field was masked-off, i.e. it was ignored in the rms averaging and source detection. It is important to note that the inner mosaic regions with high rms were not excluded from the process;

(ii) We used Blobcat, the extended source (>10 arcsec) detection and extraction software (Hales et al. 2012) first to detect and then create masks for all BCE sources in the mosaic (more details and results are given at the end of Section 3.2). Masks are applied to the channel 0 image in the same way as described in (i);

(iii) We applied BANE and Aegean algorithms (using default parameters for both packages) to the masked channel 0 image;

(iv) Only sources with flag 0 set by the Aegean finding algorithm (i.e. no fitting error reported) were used;

(v) Detected sources with S/N ratio <5 (Aegean applied detection limit) were excluded from the catalogue.

3.1.2 Sub-band images

Similarly, as in Section 3.1.1, the initial image catalogue in each band was generated by blind-fitting with default BANE and Aegean parameters. Prior to fitting, we masked each sub-band image using the same mask created in the channel 0 fitting procedure. The resulting catalogues were then cross-matched, using Topcat (Taylor 2005), against the catalogue produced in channel 0 and within an 8 arcsec radius. We examined by eye all unmatched sources (fewer

[4] https://github.com/PaulHancock/Aegean/wiki

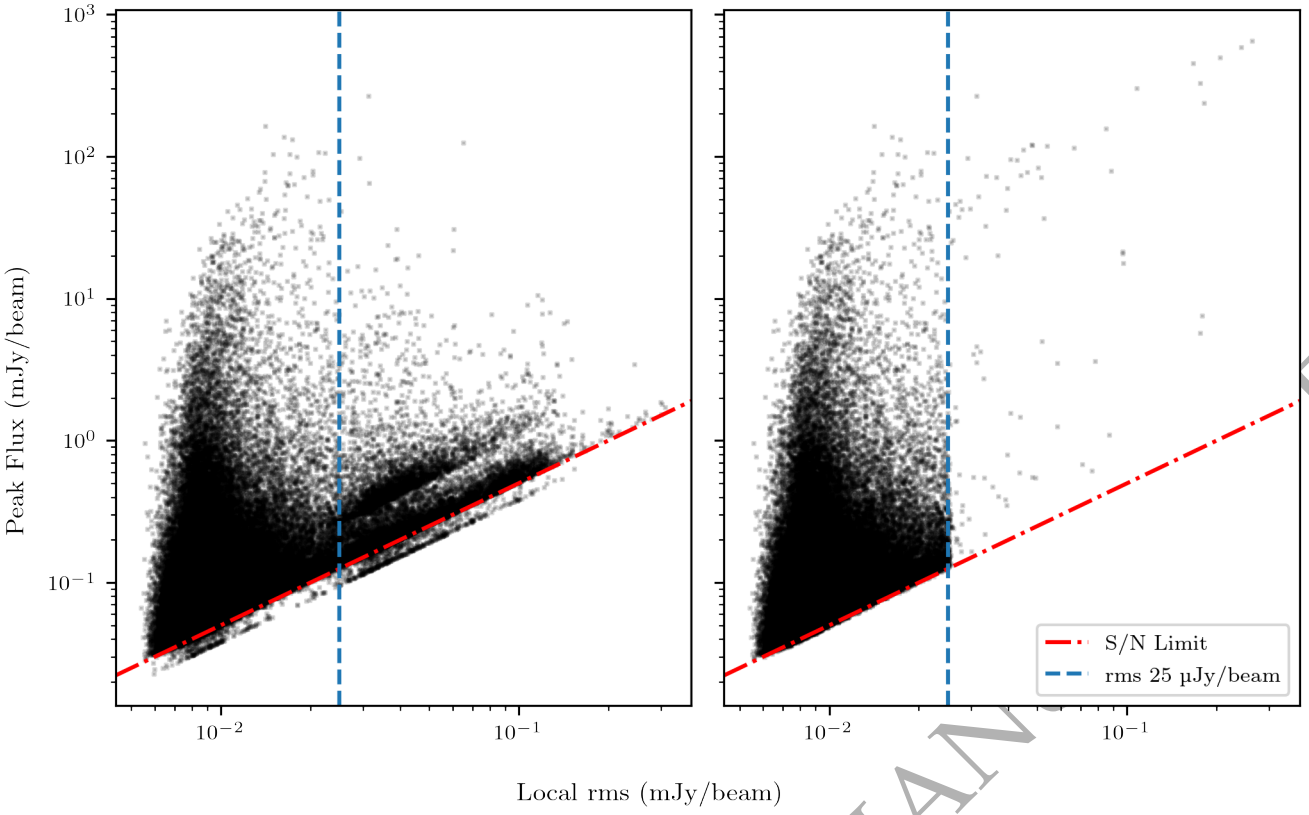

Figure 2. The plot of local rms values vs. peak flux density of the associated source from the initial catalogue of >122 000 sources (left) and the final catalogue (right). The distribution appears smooth except for a visible density excess in the region rms >25 μJy beam^{-1} (vertical blue dashed line).We point to a set of detections below the applied detection limit (S/N=5; red dash-dot line) which were deleted from the final catalogue.

Table 4. Example of the MeerKAT broad-band (1283.8 MHz) point source catalogue of 108,330 objects in the directions of the SMC with its positions, integrated flux densities with associated uncertainty, and spectral index that is calculated using other sub-band flux densities. The columns provided are as follows: (1) Source name; (2 and 3) source position; (4 and 5) source peak and integrated flux density; (6) spectral index (α) fit to all available source components with the associated error; (7) reduced χ^2_ν values obtained in the spectral index fit; (8) number of flux densities used in the spectral index fit. The full catalogue is provided through the VizieR service and as supplementary material. In the full catalogue, we also list peak and integrated flux densities for each sub-band.

Name	RA (J2000)	Dec (J2000)	$S_{\rm peak\ 1283.8\ MHz}$ (mJy beam^{-1})	$S_{\rm int\ 1283.8\ MHz}$ (mJy)	$\alpha \pm \Delta\alpha$	χ^2_ν	n
J001553–743313	00:15:52.8	–74:33:13	0.132±0.025	0.107±0.026	...	...	...
J001614–743535	00:16:13.9	–74:35:35	0.482±0.023	0.545±0.031	...	...	9
J001625–742633	00:16:24.9	–74:26:33	0.235±0.022	0.243±0.026	...	...	3
J004115–733600	00:41:14.8	–73:36:00	2.712±0.042	2.827±0.050	–0.75±0.02	0.20	12
J004347–750932	00:43:46.9	–75:09:32	1.488±0.007	1.533±0.009	0.27±0.01	0.28	12
J004516–730607	00:45:15.6	–73:06:06	1.792±0.013	1.823±0.015	–0.75±0.03	0.13	12
J004613–730704	00:46:13.2	–73:07:04	3.485±0.062	4.137±0.086	–0.82±0.02	0.09	12
J004852–731907	00:48:51.8	–73:19:07	1.455±0.047	1.454±0.054	–0.77±0.05	0.24	12
J004857–730954	00:48:57.2	–73:09:53	1.369±0.027	2.395±0.055	–0.02±0.04	0.33	12
J005049–724940	00:50:48.5	–72:49:39	1.247±0.059	1.163±0.064	–0.45±0.03	0.06	12
J005242–723621	00:52:42.2	–72:36:20	3.516±0.035	3.494±0.040	–0.70±0.02	0.20	12
J011104–731155	01:11:03.9	–73:11:55	1.473±0.015	1.522±0.018	–0.92±0.03	0.19	12
J012629–751001	01:26:29.0	–75:10:00	1.527±0.015	1.563±0.017	–0.78±0.03	0.27	12

than 100 per sub-band). Most of them appear to be artifacts at the edge of the masking regions or close to bright sources. We did not find any reliable detection in the set of unmatched sources and so they are removed (about 1100 sources) from the catalogue.

3.2 Catalogues

Our base catalogue consists of 108,330 point sources found in the broad-band 1283.8 MHz image (Table 4). The number of point sources found in each of the sub-band images is listed in Table 3.

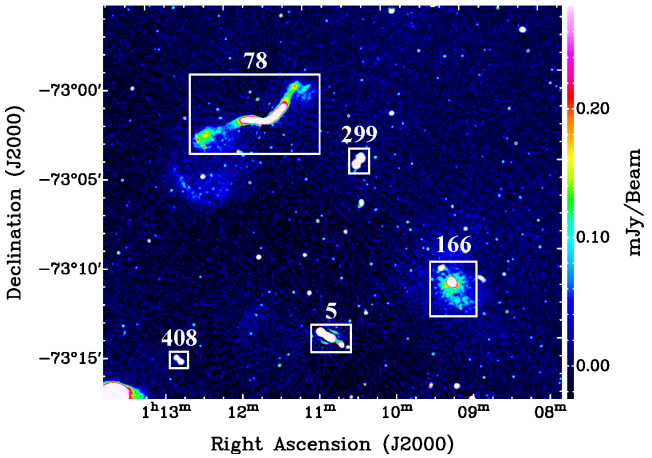

Figure 3. MeerKAT image of the SMC field showing five BCE regions. The number over each region indicates the region's ID as tabulated in Table 5.

Hancock et al. (2012) suggested that the AEGEAN detection reliability is >98 per cent at S/N>5 and 100 per cent at S/N>10. We visually inspected our catalogues and we estimate that ≈1 per cent of the catalogued sources could be false positives (artifacts).

Also, we present a catalogue of compact extended sources (BCE) detected with BLOBCAT and used for masking. We used the following parameters in the BLOBCAT detection process:

- The rms was set to a constant value of15 μJy beam^{-1}. This value was intentionally chosen to be higher than the median rms value in the image (11μJy beam^{-1}) in order to avoid collecting very faint large extended sources.
- Detection threshold was 7×RMS.
- For size limits we used >300 pixels (1 pixel = 1.5 arcsec; 7.5 arcmin) not 'thinner' along RA/Dec than 20 arcsec. Extended objects outside these size limits were filtered out.
- The edge buffer was selected to be 10 pixels (15 arcsec; i.e. two blobs can not be closer than 20 pixels or 30 arcsec).

We visually inspected the catalogue of BCE sources as the image artifacts and large extended regions (>7.5 arcmin) in the SMC bar were excluded from that catalogue. During the visual inspection, we found another 6 extended objects which were manually added to the final BCE catalogue of sources. The final catalogue contains 517 BCE objects (Table 5 and for example of BCE sources see Fig. 3). The catalogue contains an ID (as produced by BLOBCAT) and the position (RA and Dec) of the extended object's centroid. We also provide a DS9 region file (only in the electronic version of this paper) containing encapsulating regions for objects from this catalogue. Other observational parameters (e.g. classification, flux densities and angular sizes) will be published elsewhere. However, to measure flux densities of SNRs and SNR candidates (Section 4.1) we used the method described in Hurley-Walker et al. (2019a,b, Section 2.4) which includes careful region selection that excludes all obvious point sources within each given SNR.

In Fig. 4 (top) we show the point source density image based on all sources catalogued in Table 4. We investigated a 'vertical wall' of source over-density (marked with the vertical green line) and found that it corresponds to a region of excess in the weight image (Fig. 4 bottom). This is the area where we naturally pick up more sources as the exposure is deeper. This is a simple sensitivity issue, not an artifact. At the same time, this confirms that our source search software (AEGEAN; Hancock et al. 2018) is working as expected.

Table 5. Example of the catalogue of compact extended (BCE) sources. We show only the first 10 out of 517 BCE detections. We provide an ID (as produced by BLOBCAT) in Column 1 and the position of the centroid. We also provide a DS9 region file (only in the electronic version of this paper) containing encapsulating regions for objects from this catalogue.

ID	RA (J2000)	Dec (J2000)
5	01:10:48.9	–73:14:26
9	01:02:13.2	–75:46:57
10	00:42:22.3	–75:48:41
19	00:43:29.4	–70:41:48
22	01:28:12.6	–75:13:00
24	01:14:29.1	–73:21:46
27	00:38:08.6	–73:50:25
28	00:31:21.0	–70:36:48
29	00:21:50.3	–74:15:10
30	00:24:09.6	–73:57:07

Similarly, the lower source densities in the SMC bar and the Eastern Wing (Filipovic et al. 1996; Gordon et al. 2009) correspond to regions of source confusion where the software is appropriately more conservative.

3.3 Spectral indices

For all detected objects with at least two detections in sub-channel images, we can calculate a nominal spectral index α defined as $S_\nu \propto \nu^\alpha$. We use the SCIPY.ODR (Virtanen et al. 2020) code to fit the spectral index, and only accept fits that successfully converged. This produces nominal spectral index values for 40,571 objects. Following the results from recent deep radio surveys such as EMU-PS (Norris et al. 2021) and ATCA/ASKAP-LMC (Filipović et al. 2021; Pennock et al. 2021), the overall expectation is that the radio source spectral index will be in a range of –2.5< α <+1.5 where point-like active galactic nuclei (AGN) dominate the population.

We investigate the SMC MeerKAT catalogue sources' spectral index distribution obtained from sub-band flux density measurements (see Fig. 5). Not surprisingly, we find that increasing the number of sub-bands included increases the quality of the fit. Using only those sources with 12 sub-band measurements yields a mean spectral index of $\alpha = -0.65$ (STDEV=0.37), with a median of $\alpha = -0.74$ (see Fig. 6) . This is very similar to EMU-PS (Norris et al. 2021) and ATCA/ASKAP-LMC (Filipović et al. 2021; Pennock et al. 2021) results. We also note that the spectral index distribution is similar to previous results with a 'long tail' of sources with flat and inverted spectrum (0< α <1.5). We suggest that the subset of these sources with reliable spectral index values are most likely to be Gigahertz Peak Spectrum (GPS) and variable quasars (Collier et al. 2018).

However one should not forget that these flux density measurements are made within the relatively narrow bandwidth of 800 MHz, where a small change (or error) in sub-band flux density leads to large changes and unrealistic estimates in spectral index. There is a large range of unrealistic spectral index errors (0.2<$\Delta\alpha$<3) which indicates poor fitting. This is mainly for weaker sources (<1 mJy) and those with a small number of sub-band flux density measurements.

The highest-quality spectral index values arise from objects with flux density measurements in all 12 sub-bands, broad-band flux density >1 mJy, χ^2_ν<10, and $\Delta\alpha$ < 0.2. There are 2357 such sources, included in the main catalogue (Table 4) and displayed in Fig. 6. Some sources outside these constraints could have reliable spectral index values, but we are conservative in our presentation to limit contamination by unreliable values. For other point sources

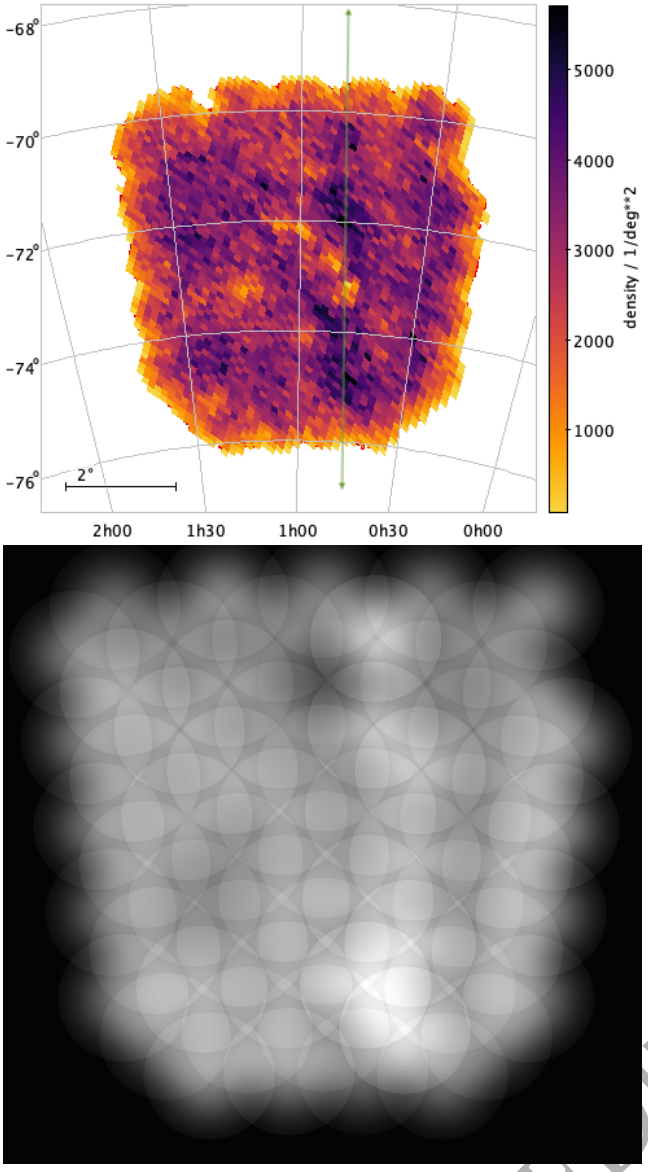

Figure 4. Top: The MeerKAT SMC field point source density image. A vertical green line indicates source overdensity. **Bottom:** The summed weight (P in Eq. 2) image, with circles indicating individual pointing positions.

of interest, the individual sub-band values should be evaluated on a case-by-case basis.

Finally, we present the spectrum for the well-known SMC SNR 1E0102–72 (MCSNR J0104–7201), an extended object with a diameter of 40 arcsec, finding consistency with previously measured flux densities (see Fig. 7 and also Alsaberi et al., in prep.). This provides some confidence in the reported flux density measurements for extended BCE sources.

3.4 Comparison with previous catalogues

3.4.1 Astrometry

We analyse our point source catalogue (Table 4) by examining the accuracy of source positions. We compared our catalogue source positions with the existing ASKAP catalogue (Joseph et al. 2019) at 1320 MHz (5652 sources) as well as the MilliQuas catalogue (see Section 2.4 and Fig. 8). We found an offset of ∼1 arcsec when compared to ASKAP (Fig. 8 middle) but excellent matching with the precise optical MilliQuas catalogue (<0.1 arcsec for 745 sources within 4 arcsec; Fig. 8 top). The offset with the ASKAP early science observations is not unexpected given that ASKAP (at the time) was still being commissioned (for more details see Joseph et al. 2019).

For radio pulsars that can be identified (all point radio sources; see Section 4.3), the MeerKAT position agrees with their timing position to the sub-arcsecond level (see Table 8).

Finally, we compare our MeerKAT catalogue with the recent Galactic ASKAP (GASKAP; Dempsey et al. 2022) survey of the SMC at 1220 MHz (bandwidth = 18.5 MHz, beam size = 8 arcsec) and its 4311 sources found using the SELAVY source finder (Whiting & Humphreys 2012). This catalogue comprises point and complex and extended (BCE) sources[5]. We found 3066 sources in common (within a search radius of 3 arcsec) and a small offset of ΔRA=–0.45 arcsec (STDEV=0.63) and ΔDEC=–0.37 arcsec (STDEV=0.62) (see Fig. 8 bottom), indicating good agreement between the two survey source positions.

3.4.2 Flux density

In Fig. 9 we show the median flux density in each channel, separately for peak and integrated flux density for all sources found in this study. This shows the varying sensitivity (depth) in each of these channels, but it also shows a trend with the frequency of the ratio of integrated-to-peak flux. This ratio is observed to diminish with frequency, which is contrary to what one might expect if more sources become resolved at a higher frequency. We suggest that the opposite is the case and more extended radio emission is included at lower frequencies.

We also compared ASKAP (Joseph et al. 2019) and MeerKAT integrated flux densities (see Fig. 10 top) for the same population of point sources in common to both surveys. We found no significant discrepancy for S/N above 50 (MeerKAT). Similarly, our comparison of flux densities for sources in common between the GASKAP and our MeerKAT catalogue indicates good matching as shown in Fig. 10 (bottom).

Our SMC MeerKAT point source catalogue flux density distributions including corresponding errors are also as expected i.e. following a power-law distribution and very similar to other recent surveys such as EMU-PS (Norris et al. 2021), ASKAP-LMC (Pennock et al. 2021) and ATCA-LMC (Filipović et al. 2021). The flux density differences compared to those of the ASKAP and GASKAP source distributions are at the ∼ ±2 per cent level.

We also show the residual image (Fig. 11), where all catalogued points sources (Table 4) have been subtracted.

4 RESULTS

Based on recent findings from ATCA and ASKAP surveys of the LMC (Filipović et al. 2021; Pennock et al. 2021), we expect that the vast majority of point radio sources catalogued here are unrelated to the SMC, with only a small number of intrinsic PNe (∼40), compact H II regions and YSOs (∼40; Oliveira et al. 2013) as well as foreground stars (∼10). This is backed up by the paucity of sources with thermal spectral indices. However, we expect that

[5] For images and tables see CASDA (`https://data.csiro.au/domain/casdaObservation/`) scheduling block 10941.

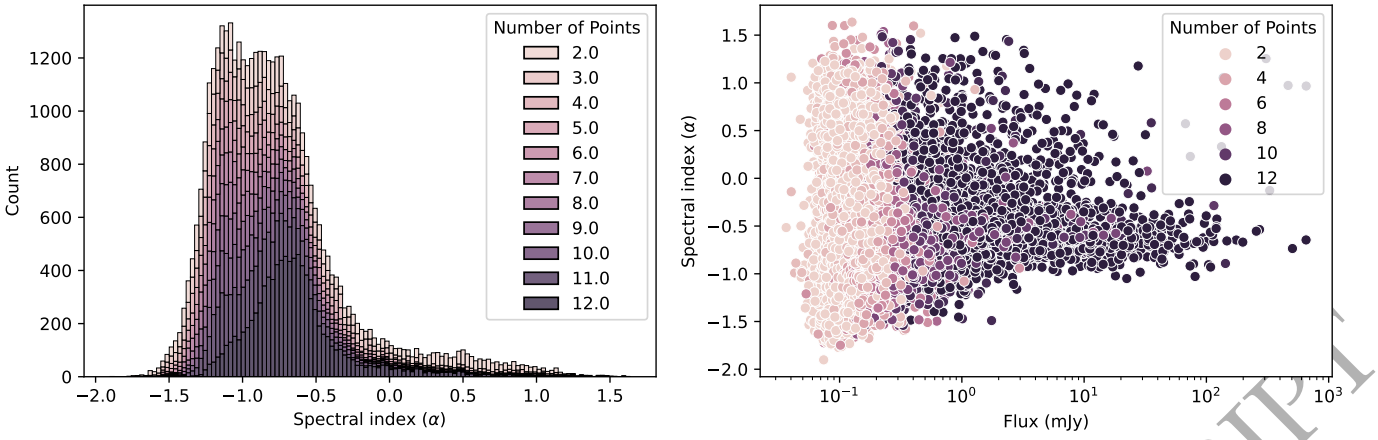

Figure 5. Left: point source spectral index distribution. This is a stacked histogram, with colour representing the number of channels used in the spectral index fit. **Right**: distribution of spectral indices per integrated flux density, with colour representing the number of channels used in the spectral index fit. In both figures, light colours represent small numbers, and dark colours represent high.

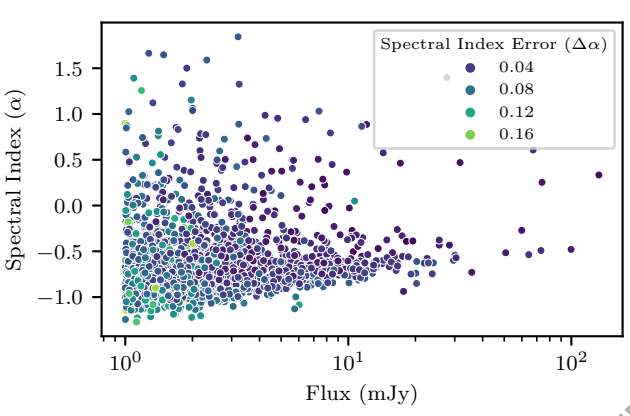

Figure 6. Distribution of spectral indices per integrated flux density for 2357 sources with 12 sub-band flux density measurements, broad-band flux density >1 mJy, χ^2_ν<10, and $\Delta\alpha < 0.2$. The colours represent the spectral index fit error according to the inset box.

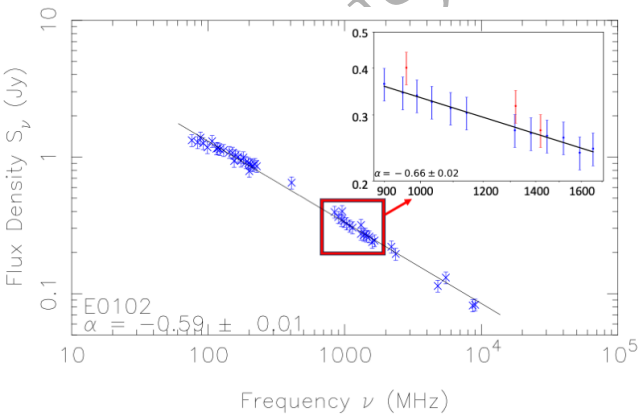

Figure 7. Radio continuum spectrum of SMC SNR 1E0102.2–7219. The red box indicates measured MeerKAT flux densities with assumed 10% uncertainty. Other flux density measurements are from Alsaberi et al. (in prep.). The best power-law weighted least-squares fit is shown (thick black line), with the spatially integrated spectral index $\alpha = -0.59 \pm 0.01$. The inset in the top right corner shows MeerKAT in-band measurements with $\alpha = -0.66 \pm 0.02$ which is in good agreement with the overall spectral index estimate. Three flux density measurements marked in red in this inset are from ASKAP and ATCA surveys.

about 50% of the 517 compact extended sources are intrinsic SMC objects such as SNRs and complex H II regions, and the other 50% are likely to be background radio AGNs with clear radio jets.

The SMC is the prime target for various multi-frequency surveys and therefore a vast amount of data is readily available for cross-comparison. Also, because the SMC is nearby and located well away from the Galactic Plane, it provides a good opportunity to study in great detail intrinsic populations of sources such as SNRs, pulsars, and PNe, alongside its ISM. The study of circularly polarised and other interesting (mainly background) sources also benefit from the breadth of available multi-wavelength data.

4.1 MeerKAT SMC SNR population

4.1.1 Previously known SMC SNRs and SNR candidates

Previous studies of SNRs in the SMC (Filipović et al. 2005; Payne et al. 2007; Filipović et al. 2008; Owen et al. 2011; Haberl et al. 2012b; Crawford et al. 2014; Roper et al. 2015; Alsaberi et al. 2019; Gvaramadze et al. 2019; Maggi et al. 2019; Joseph et al. 2019) have established 21 objects as bona fide SNRs with two more (J0106–7242 and J0109–7318)[6] considered as good candidates (see Table 6 and Figs. 12–16).

These two SNR candidates (Fig. 16) are also identified in our new MeerKAT radio images as steep radio spectrum sources ($\alpha = -0.74 \pm 0.1$ for MCSNR J0106–7242) which is indicative of non-thermal emission that is typical for SNRs. Also, we see an indication for X-ray emission from J0106–7242 in the *XMM–Newton* soft band

[6] To distinguish between SNR candidates and confirmed SNRs, Maggi et al. (2016) established a nomenclature where bona fide Magellanic Clouds (MCs) SNRs are named with the prefix 'MCSNR J' and candidates with only 'J'.

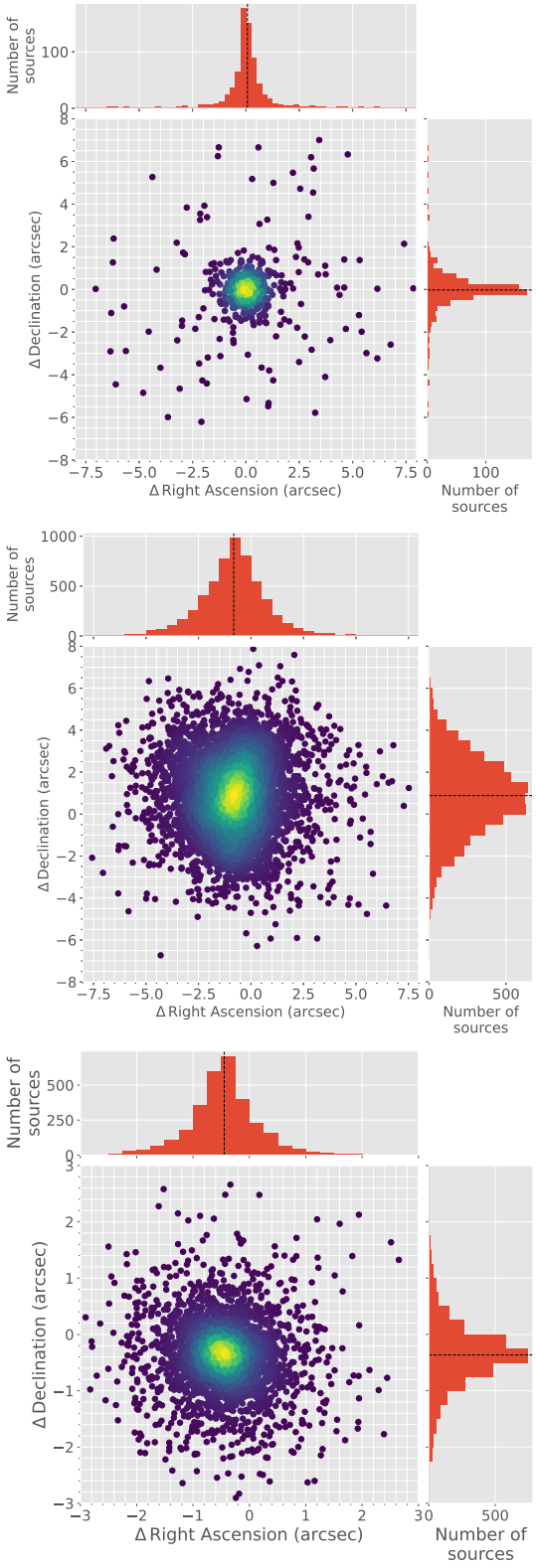

Figure 8. Top: RA and DEC offsets between MilliQuas and MeerKAT catalogues (745 sources), with mean ΔRA=+0.07 arcsec (STDEV=1.40) and ΔDEC=−0.02 arcsec (STDEV=1.33). **Middle:** Positional difference (ASKAP – MeerKAT) of 5652 sources found in both catalogues. The mean offsets are ΔRA=−0.82 arcsec (STDEV=1.59) and ΔDEC=+0.89 arcsec (STDEV=1.84). **Bottom:** Positional difference (GASKAP – MeerKAT) of 3066 sources found in both catalogues. The mean offsets are ΔRA=−0.45 arcsec (STDEV=0.63) and ΔDEC=−0.37 arcsec (STDEV=0.62).

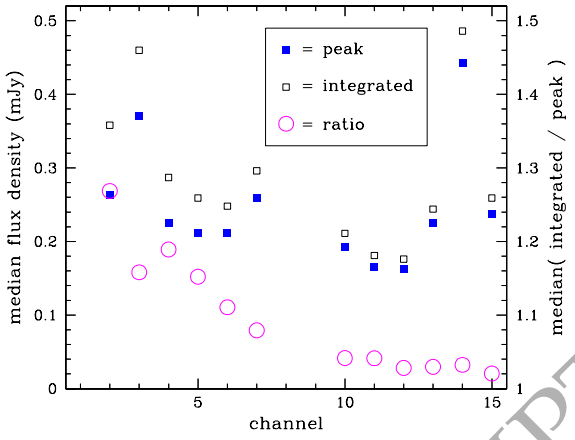

Figure 9. The median flux density in each channel, separately for peak (blue filled squares) and integrated (open squares) flux density for all sources found in this study. Note also that the variation in both peak and integrated flux density is due to varying noise levels and hence sensitivity, where noise is larger the median flux density is higher.

image and we detect J0109–7318 in optical wavebands (MCELS) with the typical SNR enhanced [S II]/Hα>0.5 ratio. Therefore, we suggest that they are now confirmed SNRs, applying the principles established in Yew et al. (2021) where bona fide SNRs must be identified (as possible SNRs) in at least two out of three (radio, optical, X-ray) wavebands.

In Tables 6 and 7 (Section 4.1.2) we show our complete radio continuum sample of the previously known SMC SNRs and new SNR candidates (see Section 4.1.2). We measure extensions, integrated flux densities and spectral index (where possible) for all 34 objects.

As our SMC SNR sample is somewhat diverse, various approaches (and initial parameters) were employed in order to measure the best SNR flux densities. We used the MIRIAD (Sault et al. 1995) task `imfit` to extract integrated flux density, extensions (diameter/axes) and position angle for each radio detected SNR. For cross-checking and consistency, we also used AEGEAN and found no significant difference in integrated flux density estimates (see Section 3.2). Namely, we measured SNR local background noise (1σ) and carefully selected the exact area of the SNR which also excludes all obvious unrelated point sources. We then estimated the sum of all brightnesses above 5σ of each individual pixel within that area and converted it to SNR integrated flux density following Findlay (1966, eq. 24). We also made corrections for an extended background where applicable i.e. for sources where nearby extended objects such as H II region(s) are evident. These non-SNR sources are also morphologically complex radio objects of a distinctively different origin (thermal emission) with their colours in our multi-wavelength RGB images (e.g., Fig. 14) set to green-to-yellow. However, for most of our SMC SNRs, this extended background flux density contribution is minimal (<5 per cent). We also estimate that the corresponding radio flux density errors are below 15 per cent as determined in our previous work (Filipović et al. 2022; Bozzetto et al. 2023). In this estimate, various contributions to the flux density error are taken into account including source overlapping of extended structures that are not part of the SNR (e.g., an AGN in the case of J0112–7304) as well as missing short spacings. Certainly, for weaker sources, this uncertainty is more pronounced while for

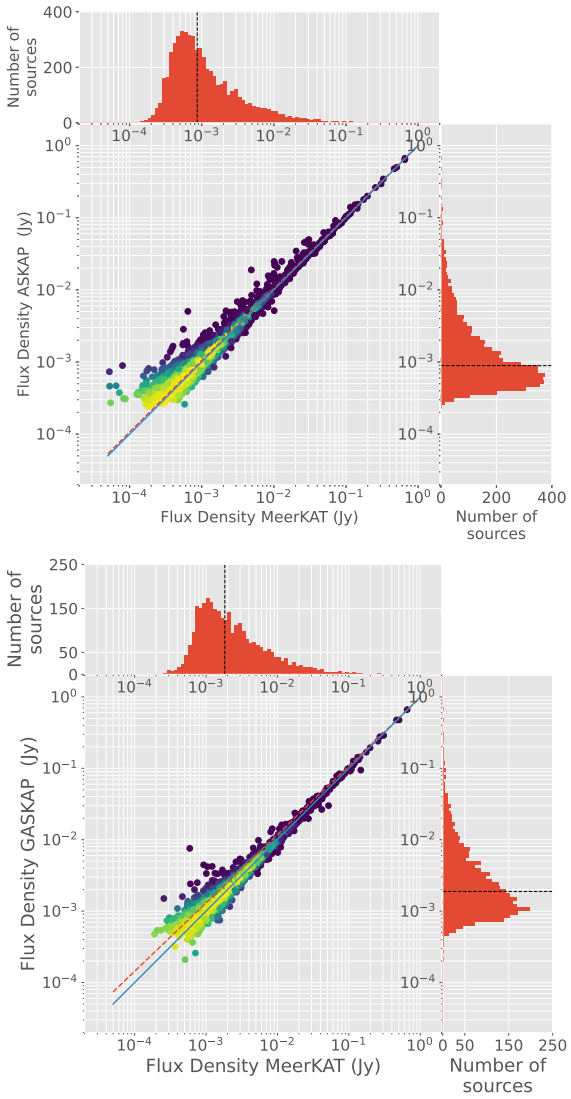

Figure 10. Top: Integrated flux density comparison of 5652 sources found in both the 1283.8 MHz (MeerKAT) and 1320 MHz ASKAP catalogues (Joseph et al. 2019). The best-fit slope (linear) is 1.016±0.001 (dashed orange) while the blue line represents a 1-to-1 ratio (see Section 3.4.2). The points are colour coded to indicate local density, yellow for high density to purple for low density. The source integrated flux density distributions are shown in the side and top panels, with the black dashed line at the median integrated flux density. **Bottom:** Integrated flux density comparison of 3066 sources found in both the 1283.8 MHz (MeerKAT) and 1420 MHz GASKAP catalogues (Dempsey et al. 2022). The best-fit slope (linear) is 0.979±0.002 (dashed orange) while the blue line represents a 1-to-1 ratio (see Section 3.4.2). The points are colour coded to indicate local density, yellow for high density to purple for low density. The source integrated flux density distributions are shown in the side and top panels, with the black dashed line at the median integrated flux density.

brighter objects such as SNR 1E0102–72 the flux density error is much smaller.

For the spectral index estimate (Table 6; Column 10), we used all available flux density measurements including ones from Maggi et al. (2019) and this work. While all our SMC SNR measurements shown in Table 6 are significant improvements, they are within the errors of previous estimates (Maggi et al. 2019).

4.1.2 New MeerKAT SMC SNR candidates and SNRs

One of our goals with the MeerKAT SMC survey is to discover new SNRs. With its unique coverage and depth, this MeerKAT survey allowed us to search for new and predominantly low surface brightness SNR candidates. At the same time, we can measure the physical properties of the already established SMC SNRs.

As MeerKAT images are sensitive to a low surface brightness and with good resolution, we can employ the same methodology described in Bozzetto et al. (2023) to search for the new SNRs. Apart from the typical morphological appearance (approximately circular shape), SNRs at radio frequencies show predominantly non-thermal emission. However, in Hα and in a majority of X-ray detections thermal emission dominates. We used the Magellanic Clouds Emission Line Survey (MCELS; Pellegrini et al. 2012) optical images as well as the new X-ray images from *XMM–Newton* (Haberl et al. 2012b) to search for new SMC SNRs. In our multi-colour/multi-waveband RGB images (Figs. 14–17) SNRs show distinctively red colour as predominantly radio emitters.

Using this method, we identified 11 new MeerKAT SMC SNR candidates (Table 7) from which one (J0100–7211; Fig. 16 top-right) we confirm as a true SNR and include in Ta-

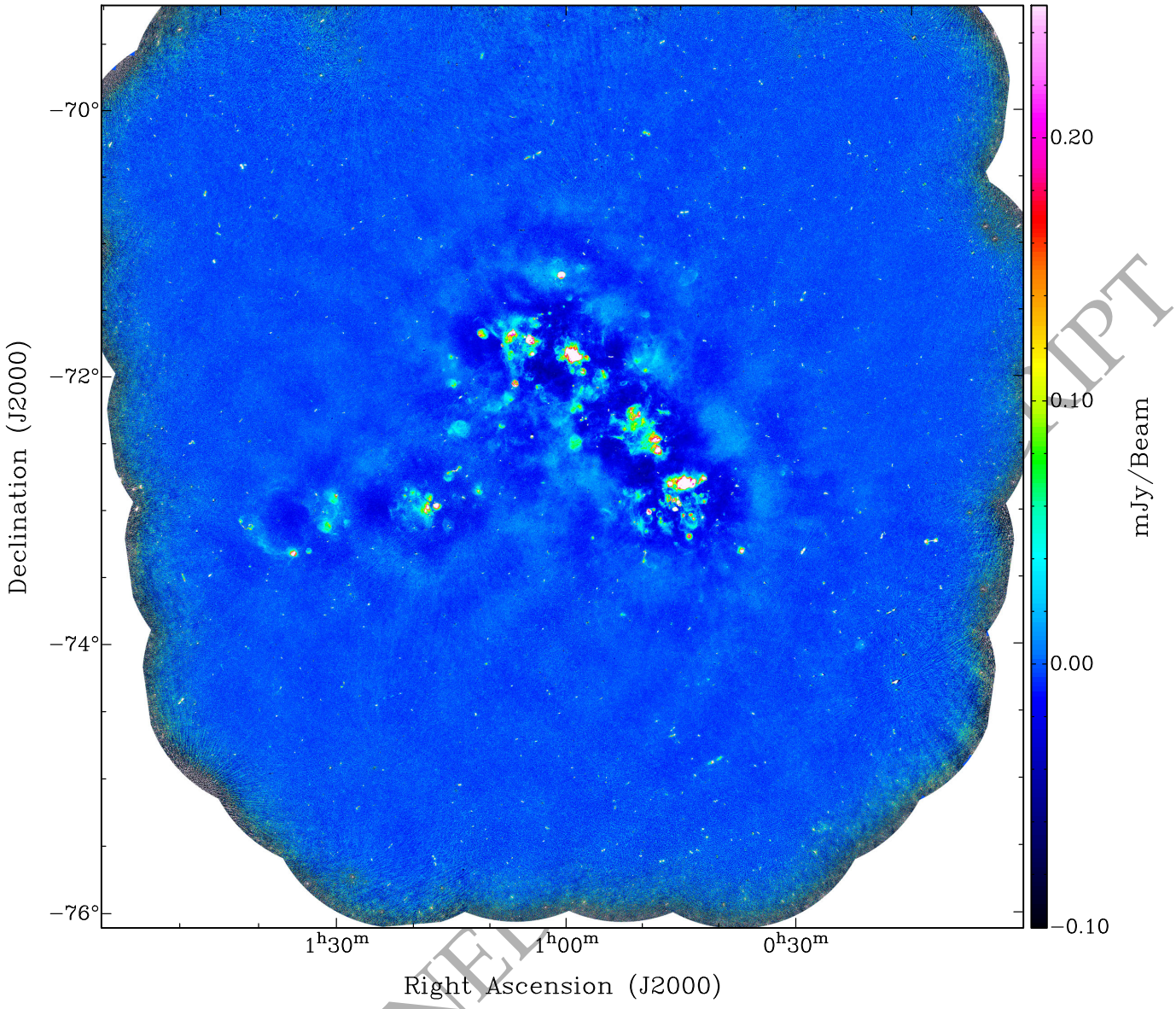

Figure 11. The MeerKAT residual image of the SMC field after subtracting all catalogued point sources listed in Table 4. The colour bar (linear scale) on the right-hand side is in units of mJy beam^{-1}.

ble 6. Apart from the typical shell-like SNR structure, MCSNR J0100–7211 also harbours the well-known X-ray magnetar (CXOU J0110043.1−721134; Lamb et al. 2002) at its centre. Several magnetars in the Milky Way are found in their parent SNR (e.g. Esposito et al. 2021), consistent with an SNR nature for this object. Multi-waveband images of the remaining 10 newly identified SMC SNR candidates are shown in Figs. 14 (one object) and 17 (nine objects).

4.1.3 SMC SNRs and SNR candidate properties

Our final sample of this MeerKAT study of SMC SNRs consists of 24 confirmed and 10 candidate remnants. Most of the new SNRs and SNR candidates display approximately semi-circular structures which together with their multi-waveband appearance are consistent with a typical SNR spherical morphology. As expected, the group of new MeerKAT SNR candidates is of low radio surface brightness (see below), which largely explains their previous non-detections.

As none of the 10 SMC SNR candidates identified here have been detected at other radio frequencies, we cannot estimate their spectral index. To compare the surface brightness of our sample

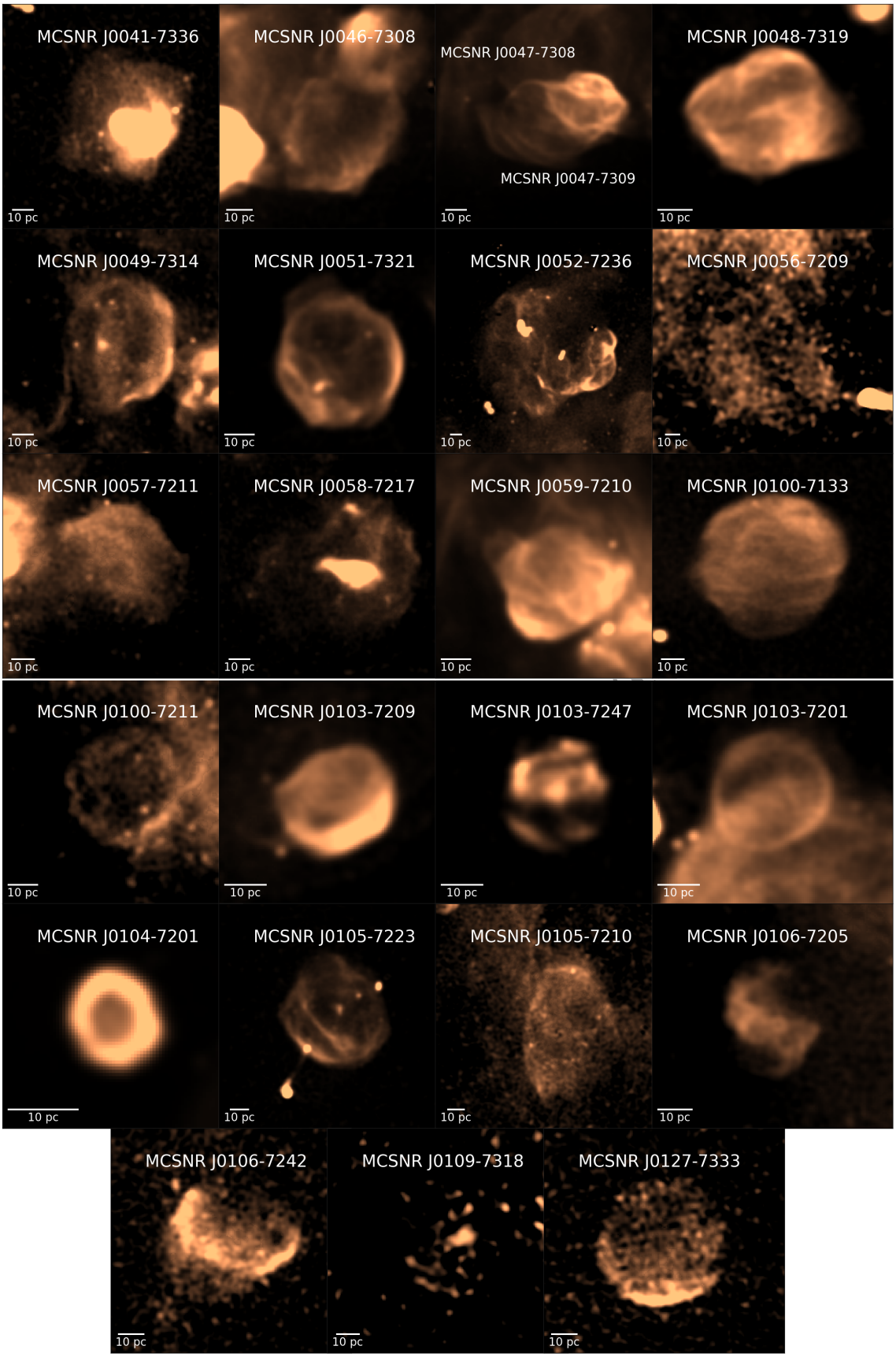

Figure 12. MeerKAT view of 24 bona fide SNRs in the SMC. Nearby point sources are subtracted in order to better see the whole SNR extent. The linear scale of 10 pc (34 arcsec at the SMC distance of 60 kpc) is shown in the bottom left corner of each panel. We use a linear intensity scale for all images.

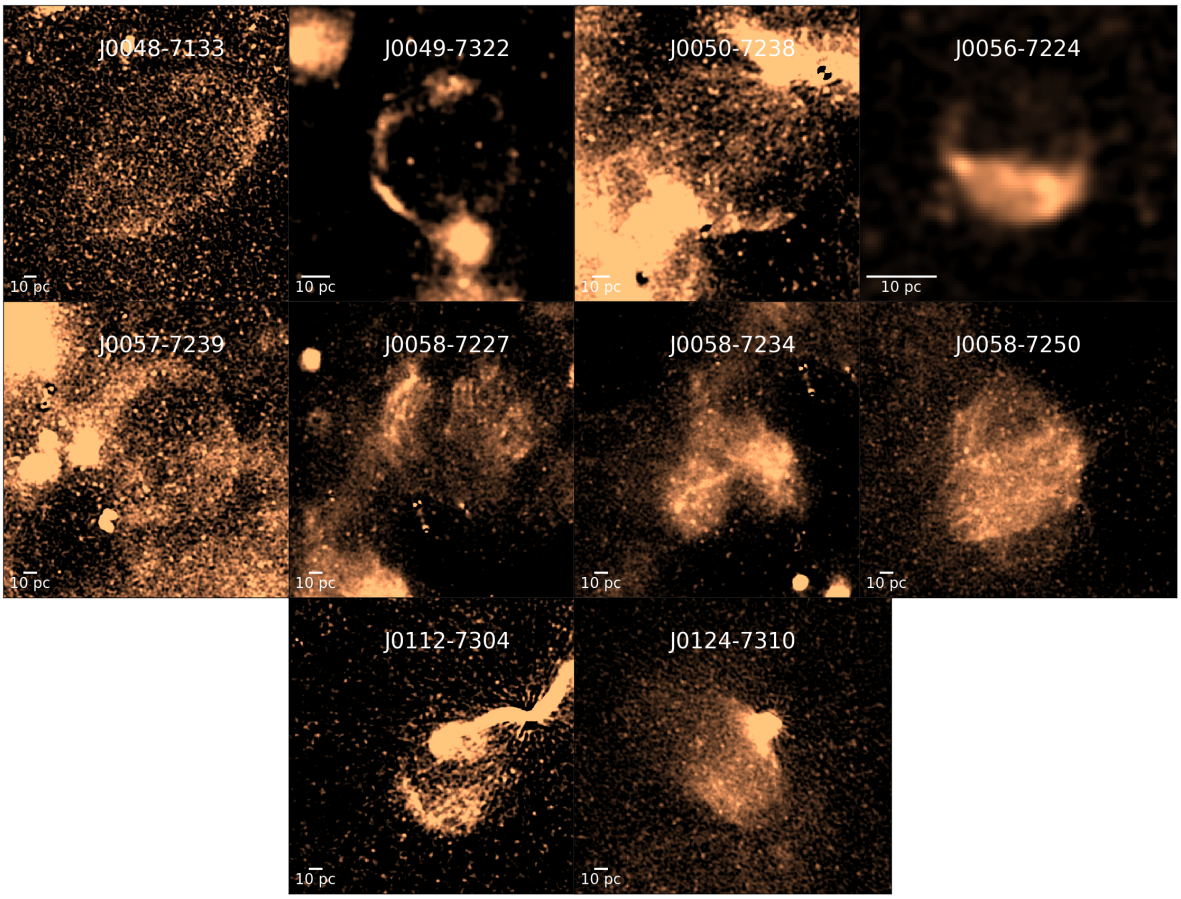

Figure 13. MeerKAT view of 10 new SNR candidates in the SMC. Nearby point sources are subtracted in order to see better the whole SNR candidate extent. The linear scale of 10 pc (34 arcsec at the SMC distance of 60 kpc) is shown in the bottom left corner of each panel. Note that the northern part of SNR candidate J0112–7304 overlaps with a background radio galaxy. We use a linear intensity scale for all images.

with established SMC SNRs (Section 4.1.1), we assumed a typical SNR spectral index of $\alpha = -0.5$ (Reynolds et al. 2012; Galvin & Filipovic 2014; Bozzetto et al. 2017; Maggi et al. 2019; Filipović & Tothill 2021a). Using this assumed spectral index allowed us to estimate the flux density and surface brightness ($\Sigma_{1\,\mathrm{GHz}}$) of these sources at 1 GHz.

These 10 new SMC SNR candidates escaped previous detection because of their low surface brightness, which typically indicates an advanced evolutionary stage. Some of these objects are most likely evolved and expanding in a rarefied environment, and we note that they occupy the bottom right portion of the SNR Σ–D diagram (Pavlović et al. 2018) as can be seen in Fig. 18.

The arithmetic average of surface brightness from the sample of 24 confirmed SMC SNRs (Table 6) is $7.1{\times}10^{-21}$ W m^{-2} Hz^{-1}sr^{-1} (median $1.4{\times}10^{-21}$ W m^{-2} Hz^{-1}sr^{-1}) while for the sample of 10 new candidates (Table 7) it is $1.6{\times}10^{-22}$ W m^{-2} Hz^{-1}sr^{-1} (median is $9.5{\times}10^{-23}$ W m^{-2} Hz^{-1}sr^{-1}). This order of magnitude difference suggests that we are discovering low surface brightness SNRs in the SMC. At the same time, our sample SNR candidate diameters are also significantly larger compared to established SMC SNRs ($D_{\mathrm{av,10\,SNRcand}}$=98 pc; STDEV=30 pc vs. $D_{\mathrm{av,24\,SNR}}$=48 pc; STDEV=19 pc). In turn, this immediately implies that our sample of 10 new objects belongs to a more evolved and mid-to-older (> 5 kyrs) SNR population (Bozzetto et al. 2017).

4.1.4 Notes on individual SMC SNRs and SNR candidates

Here, we describe properties of the SMC SNRs and SNR candidates where in our Figs. 14, 15, 16 and 17 they exhibit mainly red colour.

4.1.4.1 SMC SNRs: DEM S5 (Fig. 14; Alsaberi et al. 2019, also see in Carli et al. (in prep.)) and IKT 16 (Fig. 15; Maitra et al. 2021, 2015; Owen et al. 2011; Carli et al. 2022) contain the only two confirmed Pulsar Wind Nebulae (PWN) in the SMC. [HFP2000] 334 (Fig. 15; Crawford et al. 2014) and recently 1E 0102.2–7219 (Alsaberi et al. 2022, submitted) were also examined for the existence of a PWN but without a firm confirmation. Finally, SNRs MCSNR J0127–7333 (Fig. 16; Haberl et al. 2012a), MCSNR J0103–7201 (Fig. 15) and the here discovered MCSNR J0100–7211 (Fig. 16) were found around well-known X-ray pulsars (the Be/X-ray binaries SXP 1062 and SXP 1323, and the magnetar CXOU J0110043.1−721134). The existence of a neutron star at the centre of an SNR with a circular ring-like shell establishes its core-collapse origin. The distinctive circular radio appearance of MCSNR J0100–7211 and its central magnetar makes this object a new bona fide SNR, despite the fact that no X-ray emission from the SNR itself could be detected yet.

Three SNRs in the N 19 region (Fig. 14 top-right; [HFP2000] 414, IKT 2 and DEM S32) are clearly overlapping. Defining their borders (and properties) is quite difficult, but we manage to measure the properties consistent with their SNR nature.

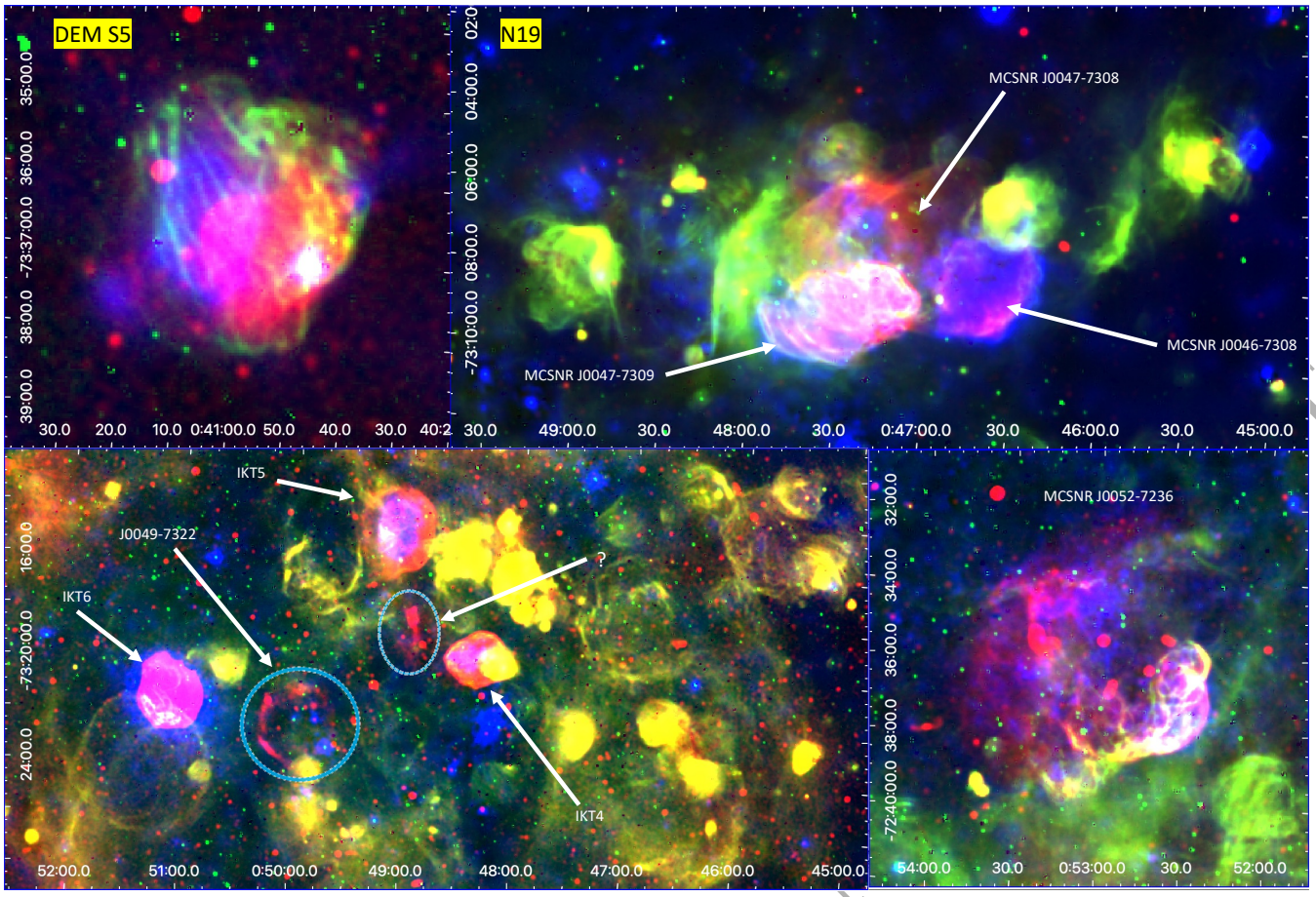

Figure 14. RGB images of selected SMC regions. R corresponds to MeerKAT 1.3 GHz emission (plotted using a linear transfer function), G is Hα (MCELS) and B is 0.3–1 keV X-rays from *XMM–Newton*. This image helps to discriminate between SNRs (dominantly in red colour) and other objects such as H II regions. Red dots are radio point sources of predominantly background nature but some PNe, pulsars and foreground stars are seen as well. We show in these multi-colour/multi-band images well known SMC SNRs (Table 6) DEM S5 (top left), N 19 region SNRs (top-right; MCSNR J0046–7308, MCSNR J0047–7308 and MCSNR J0047–7309), south of N 19 region SNRs (bottom-left; IKT 4, IKT 5 and IKT 6) and MCSNR J0052–7236 (bottom right). In the bottom-left image, we show the new MeerKAT SNR candidate J0049–7322 (marked with a cyan dashed circle) and also a newly discovered mysterious source (marked with '?' and cyan dashed ellipse).

The region south from N 19 (Fig. 14 bottom-left) consists of three previously confirmed SNRs (IKT 4, IKT 5 and IKT 6). Here we propose a new SNR candidate J0049–7322 which shows a filamentary ring structure. Interestingly, there is some indication for a similar structure seen on the *XMM–Newton* mosaic image, which needs confirmation by a dedicated future observation.

The previously confirmed MCSNR J0052–7236 (DEM S68; Fig. 14 bottom-right) looks much more extensive in our new radio images (and also in the *XMM–Newton* soft X-ray images) than previously defined in Vardoulaki et al. (2019). Especially its northern end makes this SNR among the largest D_{av}=88.2 pc.

Well-established SNRs N 66D, IKT 18, DEM S108, IKT 23 (Fig. 15) and IKT 21, DEM S128 (Filipović et al. 2000) and IKT 25 (Fig. 16) show typical SNRs characteristics. Three low surface brightness confirmed SNRs include MCSNR J0056–7209 and here confirmed MCSNR J0106–7242 and MCSNR J0109–7318.

4.1.4.2 SMC SNR candidates: Our 10 new SMC SNR candidates (Fig. 17) are exclusively seen at radio continuum frequencies. However, in a few candidates such as for J0048–7133 ([S II]) and J0112–7304 ([O III]) we can see some possible traces of corresponding optical emission in the MCELS images. The shape of SNR candidate J0048–7133 is elongated and with a major axis of ~180 pc might represent one of the largest SNRs that expands in the rarefied environment as it is located some 0.75 degree from the main body of the SMC. This might be a similar type of SNR to our recent discovery of the intergalactic SNR MCSNR J0624–6948 (Filipović et al. 2022) or MCSNR J0509–6402 (Yew et al. 2021). Besides J0049–7322 (see above) there is also some faint diffuse X-ray emission indicated in *XMM–Newton* images at the location of J0124–7310. Again, a dedicated observation is required for confirmation. Among these 10 new SNRs candidates, we detect three large-scale objects (J0050–7238, J0057–7239 and J0058–7250) with diameters exceeding 100 pc. While somewhat unlikely, they also might represent (super)bubbles (Yamane et al. 2021; Kavanagh et al. 2019; Sano et al. 2017). SNR candidate J0112–7304 is 'hidden' around the southeast jet of the nearby large (apparent) AGN and therefore its true extent might be somewhat different than measured here.

4.2 Automating the SNR search

Scientific interpretation of diffuse emission from the ISM generally requires constraining the emission mechanism. A common calcu-

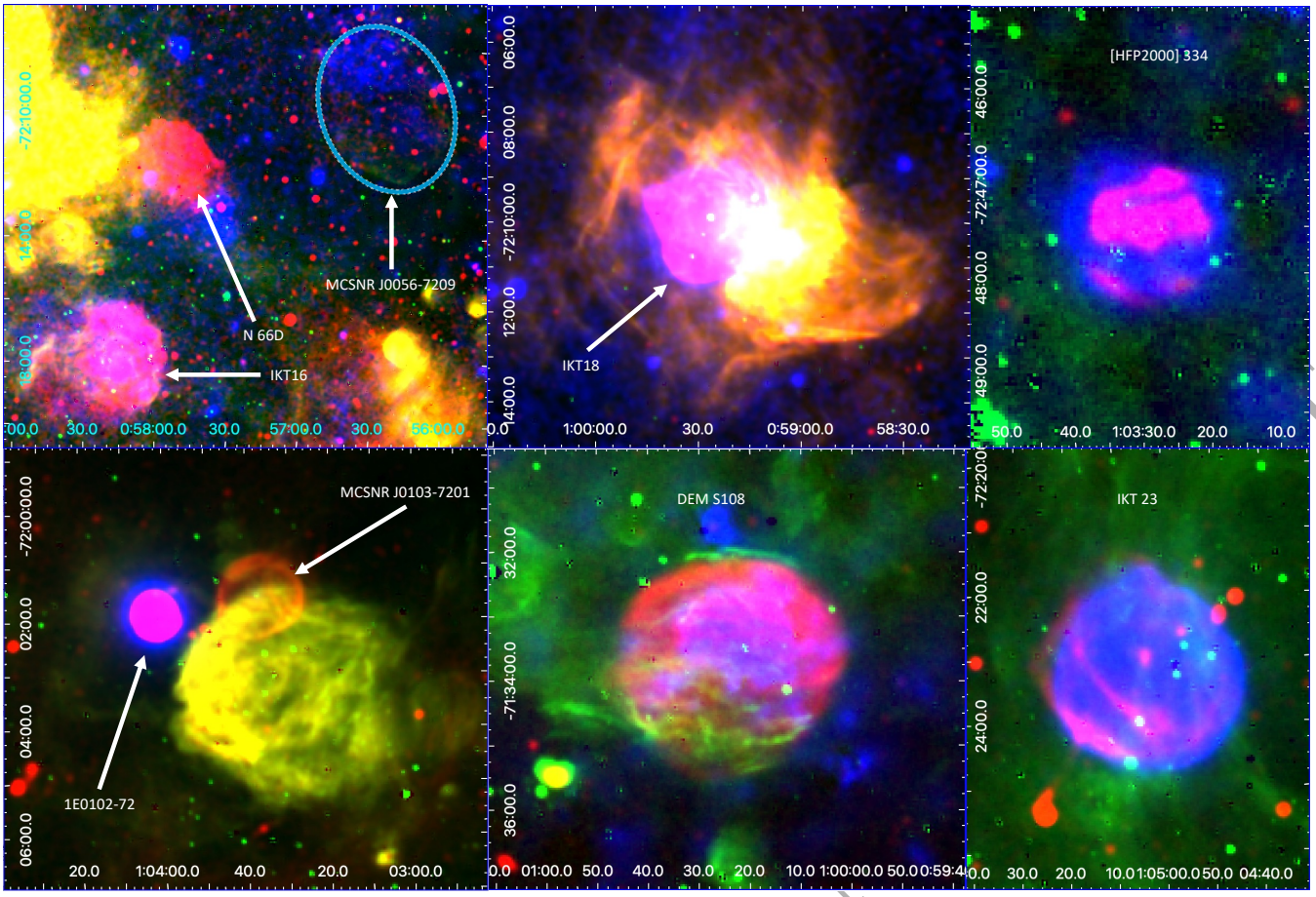

Figure 15. Same as Fig. 14. We show in these multi-colour/multi-band images well known SMC SNRs (Table6): IKT 16, N 66D and MCSNR J0056–7209 (top-left), IKT 18 (top-middle), [HFP2000] 334 (top-right), 1E0102–72 and MCSNR J0103–7201 (bottom-left), DEM S108 (bottom-middle) and IKT 23 (bottom-right).

lation in the centimetre continuum regime is the spectral index (α), which can discriminate between optically thin thermal free-free (α ~–0.1) and non-thermal (α <–0.5), or even contributions from optically thick free-free, or dust emission with larger positive spectral indices. Spectral indices calculated over modest frequency ranges have large uncertainties, and any differences in spatial filtering or primary beam response as a function of frequency only increase the uncertainties. The thermal/non-thermal fraction can also be fitted with spectral data, with similarly large uncertainties. Even with MeerKAT's large fractional bandwidth, these calculations are challenging.

SNRs can be identified visually as described in Section 4.1. Although such identification is relatively unambiguous for an experienced investigator, it is desirable to explore more automated techniques, especially in the era of large-scale surveys. Thermal and non-thermal sources have different correlations between infrared and centimetre emission, so the ratio has been used to distinguish between emission mechanisms (Broadbent et al. 1989; Cohen et al. 2007). We extend the use of a single infrared map to use infrared maps at several frequencies and a map of Hα, which is also expected to correlate strongly with thermal centimetre emission, and rather less strongly with non-thermal emission. We first preprocess the maps to have the same spatial filtering characteristics, then demonstrate a supervised and unsupervised classification in the SMC.

For the analysis of diffuse emission, we use the residual MeerKAT image produced by AEGEAN by removing all of the compact and point sources (see Section 3.4.2). This is not essential, and similar results can be achieved with the original image, but does make the preprocessing (see next section) easier, and helps highlight the extended sources. We complement MeerKAT with images that trace the physically most relevant emission mechanisms: emission from warm dust is traced by *Spitzer* MIPS 24 μm at native 6 arcsec resolution from the SAGE survey (Meixner et al. 2006); and somewhat cooler dust by *Herschel* PACS 160 μm at 13 arcsec resolution from the HERITAGE survey (Meixner et al. 2013). Although longer wavelength *Herschel* data are available, it is desirable to perform this analysis at as close to the MeerKAT resolution as possible. Free-free emission from ionised gas, albeit subject to dust attenuation, is traced by MCELS continuum-subtracted Hα (Winkler et al. 2015).

4.2.1 *Image preprocessing*

At the time of publication, appropriately deep wide-band single-dish observations of the SMC did not exist, so as with all interferometer data, the MeerKAT image lacks short spacing information, evident in negative bowls around bright emission at large angular scales. As is well known, there is no way to reliably extrapolate the interferometer measurements to zero *uv* distance and recover the unmeasured information on those large angular scales. However, any correlation

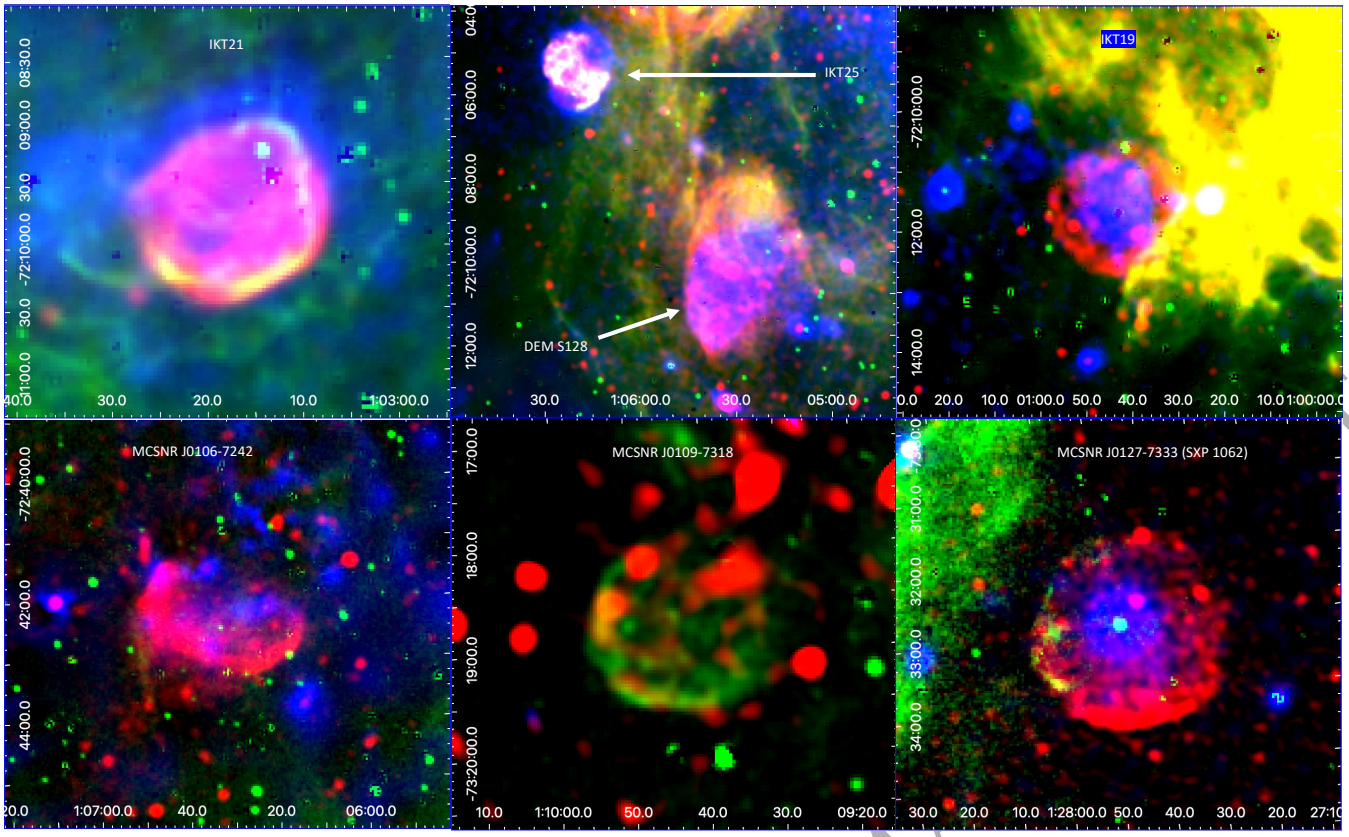

Figure 16. Same as Fig. 14. We show in these multi-colour/multi-band images well known SMC SNRs (Table6): IKT 21 (top-left), IKT 25 and DEM S128 (top-middle), IKT 19 (top-right), MCSNR J0106–7242 (bottom-left), MCSNR J0109–7318 (bottom-middle) and SXP 1062 (bottom-right).

Table 6. 24 confirmed SNRs in the SMC. The errors on the integrated flux densities (Column 9) are estimated to be <15%. Column 3 abbreviations are: DEM S: Davies et al. (1976), [HFP2000]: Haberl et al. (2000), IKT: Inoue et al. (1983), SXP: Haberl et al. (2012a). Position angle in Column 8 is measured from north to east. In Column 11 we list SNR surface brightness at 1 GHz where results in brackets assumed a typical SNR spectral index of –0.5. In Column 12 we indicate radio, X-ray and/or optical ([S II] or [O III]) detection. Along with the MCSNR Name (Column 2) we mark with * newly promoted bona fide SNRs in this study. Names in column (3) marked with † are names of associated central X-ray point sources. The assumed distance to the SMC is 60 kpc.

No.	MCSNR Name	Other Name	RA (J2000)	DEC (J2000)	$D_{maj} \times D_{min}$ (arcsec)	D_{av} (pc)	PA (°)	$S_{1283.8\,MHz}$ (Jy)	$\alpha \pm \Delta\alpha$	Σ_{1GHz} ($\times 10^{-20}$) (W m^{-2}Hz^{-1}sr^{-1})	Notes	Fig.
(1)	(2)	(3)	(4)	(5)	(6)	(7)	(8)	(9)	(10)	(11)	(12)	(13)
1	J0041–7336	DEM S5	00 41 01.7	−73 36 30.4	246×220	68	105	0.1560	–0.28±0.01	0.141	R, X, O	14
2	J0046–7308	[HFP2000] 414	00 46 40.6	−73 08 14.9	185×140	47	35	0.1012	–0.37±0.04	0.244	R, X, O	14
3	J0047–7308	IKT 2	00 47 16.6	−73 08 36.5	110×100	31	45	0.3537	–0.54±0.03	2.410	R, X, O	14
4	J0047–7309	DEM S32	00 47 36.5	−73 09 20.0	180×120	43	75	0.2594	–0.58±0.11	0.556	R, X, O	14
5	J0048–7319	IKT 4	00 48 19.6	−73 19 39.6	165×130	43	90	0.1071	–0.59±0.03	0.345	R, X, O	14
6	J0049–7314	IKT 5	00 49 07.7	−73 14 45.0	190×190	55	0	0.0416	–0.66±0.05	0.080	R, X, O	14
7	J0051–7321	IKT 6	00 51 06.7	−73 21 26.4	145×145	42	0	0.1008	–0.55±0.03	0.276	R, X, O	14
8	J0052–7236	DEM S68	00 52 59.9	−72 36 47.0	340×270	88	135	0.0939	–0.52±0.03	0.055	R, X, O	14
9	J0056–7209		00 56 28.1	−72 09 42.2	340×225	81	30	0.0065	(–0.5)	(0.005)	R, X, O	15
10	J0057–7211	N 66D	00 57 52.4	−72 11 49.7	199×161	52	40	0.0290	–0.72±0.03	0.052	R, O	15
11	J0058–7217	IKT 16	00 58 22.4	−72 17 52.0	267×241	74	0	0.0707	–0.51±0.03	0.071	R, X, O	15
12	J0059–7210	IKT 18	00 59 27.7	−72 10 09.8	140×140	41	0	0.4810	–0.47±0.02	1.520	R, X, O	15
13	J0100–7133	DEM S108	01 00 23.9	−71 33 41.1	240×216	66	0	0.1741	–0.50±0.02	0.197	R, X, O	15
14	J0100–7211*	CXOU J0110043.1 −721134†	01 00 44.3	−72 11 40.9	121×124	66	0	0.0070	(–0.5)	(0.034)	R	16
15	J0103–7209	IKT 21	01 03 17.0	−72 09 42.5	95×83	26	135	0.0806	–0.67±0.03	0.670	R, X, O	16
16	J0103–7247	[HFP2000] 334	01 03 29.1	−72 47 32.6	105×85	28	0	0.0288	–0.58±0.05	0.190	R, X	15
17	J0103–7201	SXP 1323†	01 03 36.6	−72 01 35.1	98×83	26	90	0.0410	(–0.5)	(0.109)	R, X, O	15
18	J0104–7201	1E 0102.2–7219	01 04 01.2	−72 01 52.3	43×45	13	0	0.2970	–0.67±0.01	9.670	R, X, O	15
19	J0105–7223	IKT 23	01 05 04.2	−72 23 10.5	192×192	56	0	0.0778	–0.61±0.03	0.155	R, X	15
20	J0105–7210	DEM S128	01 05 30.5	−72 10 40.4	184×126	44	0	0.0499	–0.55±0.03	0.138	R, X	16
21	J0106–7205	IKT 25	01 06 17.5	−72 05 34.5	110×80	27	25	0.0101	–0.41±0.04	0.062	R, X, O	16
22	J0106–7242*		01 06 33.7	−72 42 29.5	175×153	48	10	0.0126	–0.74±0.10	0.036	R, X	16
23	J0109–7318*		01 09 43.6	−73 18 46.0	105×105	31	0	0.0154	(–0.5)	(0.086)	R, O	16
24	J0127–7333	SXP 1062†	01 27 44.1	−73 33 01.6	166×166	48	0	0.0100	–0.42±0.12	0.015	R, X, O	16

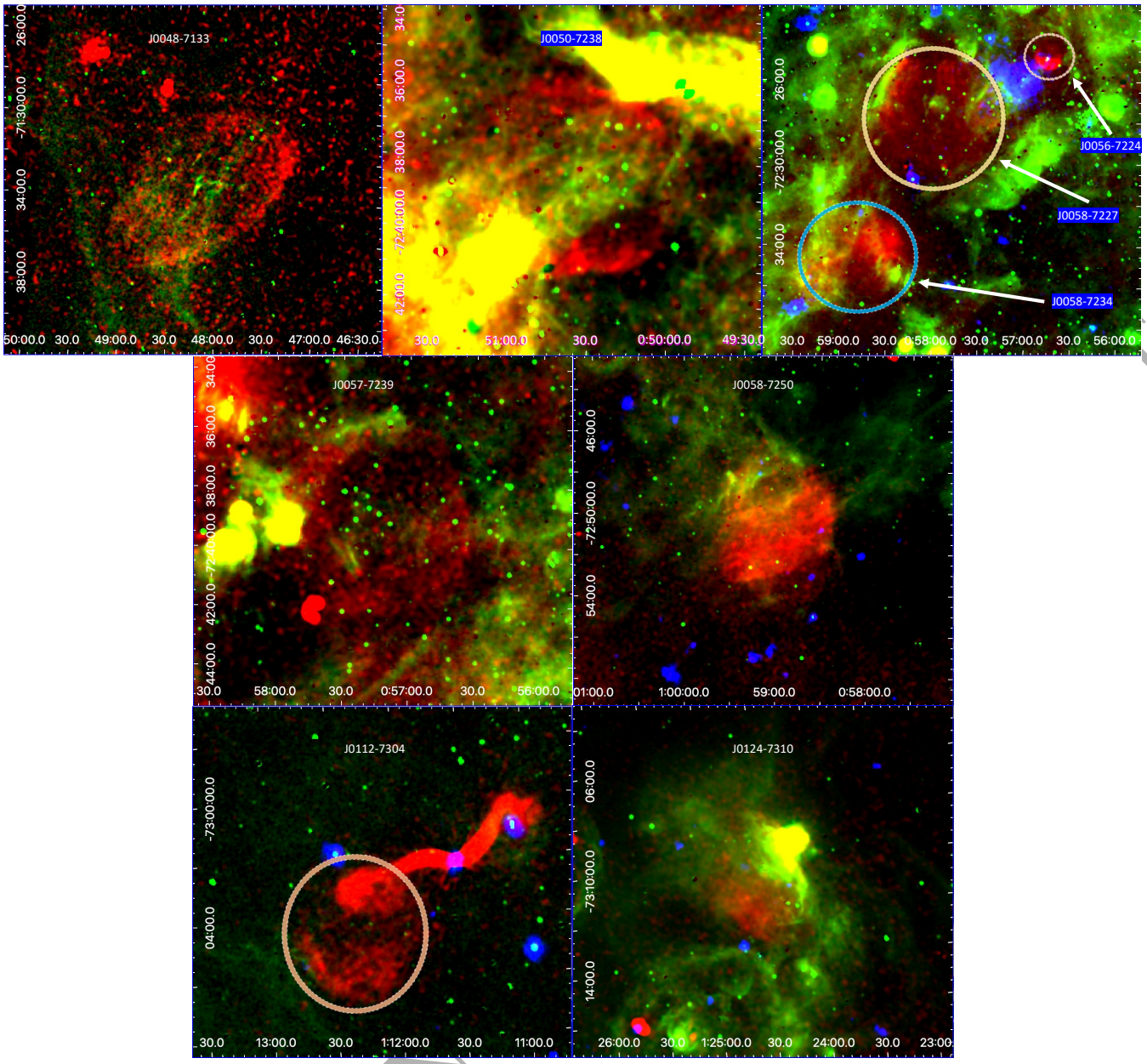

Figure 17. Same as Fig. 14. We show in these multi-colour/multi-band images new MeerKAT SMC SNRs candidates (Table7): J0048–7133 (top-left), J0050–7238 (top-middle), J0056–7224, J0058–7227 and J0058–7234 (top-right), J0057–7239 (middle-left), J0058–7250 (middle-right), J0112–7304 (bottom-left) and J0124–7310 (bottom-right). The MeerKAT SNR candidate J0049–7322 is shown in Fig. 14.

calculation with multiwavelength data would be stymied by these negative bowls, so we remove them cosmetically, using a method similar to the negative of the 'feather' technique long used for the combination of interferometer and single dish data (Stanimirovic et al. 1999; Hughes et al. 2007; Cotton 2017). We performed the calculation on 2200×2200 pixel overlapping tiles separated by 2000 pixels, but varied both the tile and overlap size and found minimal differences in the output (the pixel scale is 1.5 arcsec, so the tiles are 0.92 degree on a side). A robust rms is calculated in two iterations: a first σ is calculated from the MAD (Median Absolute Deviation), then again from all pixels less than 15 times the first estimate. Then all pixels greater than $2.5\times\sigma$ are set to zero. Each tile image is padded by another 200 pixels on all sides, extending the edge values outwards, for numerical stability, Fourier transformed, and all but the ±7 pixels corresponding to angular scales with wavelengths from DC to (2400/7)×0.92 deg = 5.3 arcmin are zeroed. We keep a sharp cutoff in Fourier space because the goal is to remove the existing ringing/bowls. That low-pass-filtered image is inverse Fourier transformed and subtracted from the original mosaic. The resulting 'background-subtracted' tiles are mosaiced back together with a linear weighting of the overlap regions. The original and 'cosmetically flattened' MeerKAT images of the SMC are shown in Figure 19. As with the tile size, we varied the number of pixels to keep in the background image, and whether the cutoff is sharp or slightly tapered and chose values to minimise large-scale bowling without affecting the surface brightness of real sources.

In order to compare multiwavelength images and analyse the

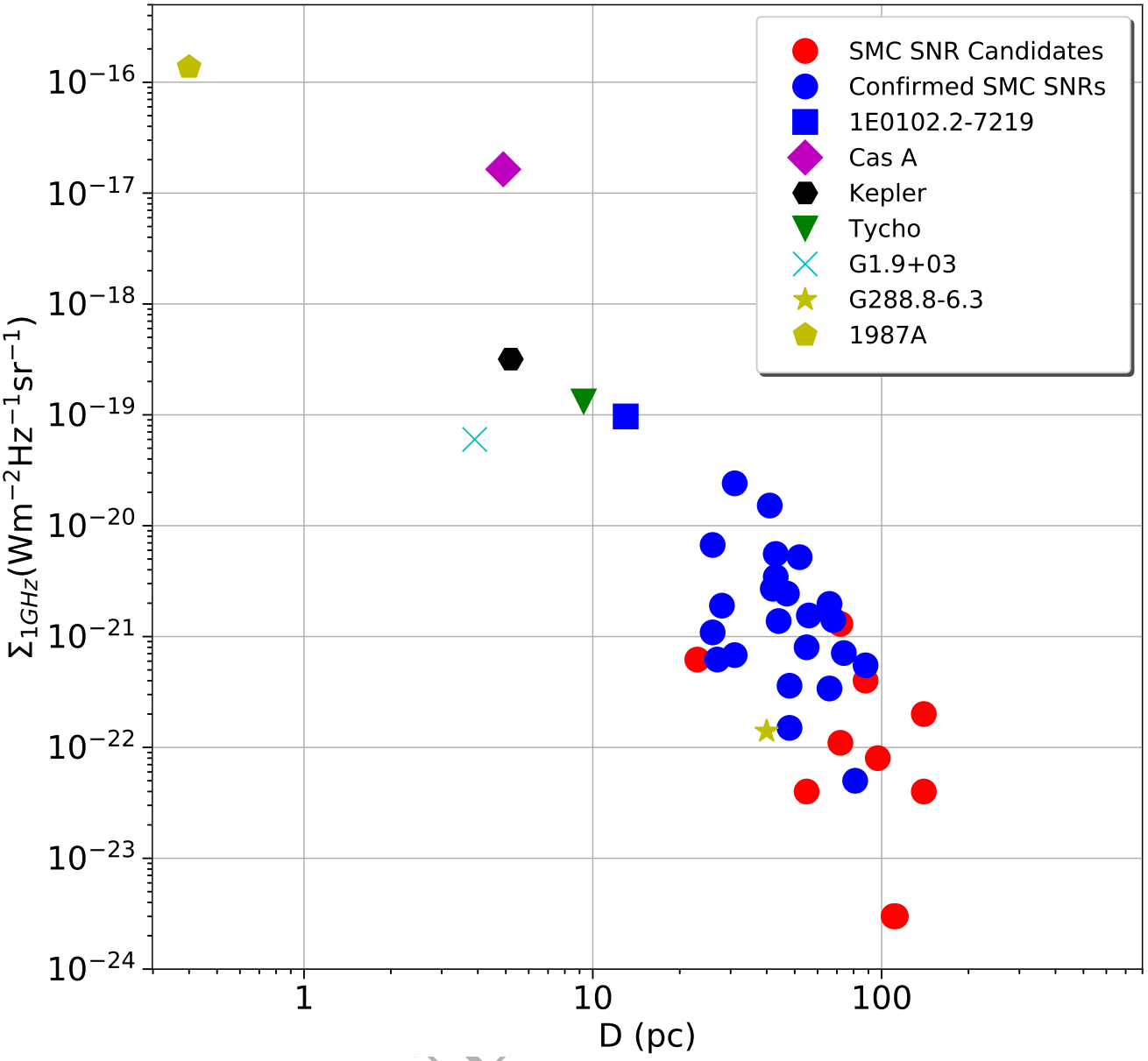

Figure 18. Radio surface brightness–to–diameter diagram for the 24 SMC SNRs (blue circles) and 10 candidates (red circles) at a frequency of 1 GHz (see Tables 6 and 7. We also use several estimates of known Galactic SNRs from Pavlović et al. (2018) as well as G288.8–6.3 (Filipović et al. 2023, marked with a yellow star in the bottom right corner) which is one of the lowest Galactic radio surface brightness SNR. Cassiopeia A is shown with a magenta-filled diamond while the cyan cross represents the youngest Galactic SNR, G1.9+0.3 (Luken et al. 2020). We also included Kepler SNR (black hexagon), Tycho (green triangle) and SN 1987A (yellow pentagon).

same range of angular scales, we must impose the same filtering on those images as well.

4.2.2 *Colour index*

Next, we analyse the pixel-by-pixel colours (flux ratios) involving centimetre, Hα, 24 μm and 160 μm wavelengths. Figure 20 shows the pixel colour distributions of the previously known SNRs (Table 6) and known SMC H II regions (Davies et al. 1976). The colour separation is very robust to different choices of large-spatial-scale filtering (including not doing any filtering at all on images other than the centimetre interferometric one), to modest changes in the training sets of objects, to different signal-to-noise thresholds, and even to smoothing the images up to 1 arcmin resolution. We calculate the best-discriminating line between the populations using a linear kernel support vector machine, specifically LinearSVM in scikit-learn (Pedregosa et al. 2011). Then for each pixel in the map, the perpendicular distance from its colours to that line defines a colour index (see Fig. 20). Quantitatively,

$$\begin{aligned} x &= \log(F_{24\mu m}/|F_{160\mu m}|); \\ y &= \log(F_{cm}/|F_{H\alpha}|); \\ \text{dividing line } y &= 0.7x - 2.6; \\ \text{color index } ind &= \frac{-0.7x + y + 2.5}{\sqrt{0.7^2 + 1}}. \end{aligned}$$

Of the 24 confirmed SNRs, 19 have sufficient signal-to-noise

Table 7. Ten new MeerKAT SNR candidates in the SMC. The errors on the integrated flux densities (Column 8) are estimated to be <15%. In Column 10 we list SNR candidate surface brightness at 1 GHz where we assumed a typical SNR spectral index of –0.5. In Column 11 we indicate radio, X-ray and/or optical ([S II] or [O III]) detection. The assumed distance to the SMC is 60 kpc.

No.	Candidate Name	RA (J2000)	DEC (J2000)	$D_{maj} \times D_{min}$ (arcsec)	D_{av} (pc)	PA (°)	$S_{1283.8\,MHz}$ (Jy)	α	Σ_{1GHz} ($\times 10^{-20}$) (W m^{-2}Hz^{-1}sr^{-1})	Notes	Fig.
(1)	(2)	(3)	(4)	(5)	(6)	(7)	(8)	(9)	(10)	(11)	(12)
1	J0048–7133	00 48 14.4	−71 33 28.7	625×370	140	120	0.0174	(–0.5)	0.004	R, O?	17
2	J0049–7322	00 49 57.1	−73 22 23.7	188×188	55	0	0.0026	(–0.5)	0.004	R, X?	14
3	J0050–7238	00 50 35.3	−72 38 38.3	356×314	97	0	0.0158	(–0.5)	0.008	R	17
4	J0056–7224	00 56 46.1	−72 24 49.8	80×75	23	0	0.0060	(–0.5)	0.062	R	17
5	J0057–7239	00 57 14.5	−72 39 13.7	378×378	110	0	0.0007	(–0.5)	0.0003	R	17
6	J0058–7227	00 58 00.1	−72 27 56.2	387×382	112	0	0.0008	(–0.5)	0.0003	R	17
7	J0058–7234	00 58 53.7	−72 34 40.4	348×262	88	100	0.0605	(–0.5)	0.040	R	17
8	J0058–7250	00 58 57.0	−72 50 46.2	512×452	140	100	0.0760	(–0.5)	0.020	R	17
9	J0112–7304	01 12 18.8	−73 04 23.8	296×206	72	0	0.0133	(–0.5)	0.013	R, O?	17
10	J0124–7310	01 24 30.7	−73 10 33.0	292×208	72	0	0.0107	(–0.5)	0.011	R, X?	17

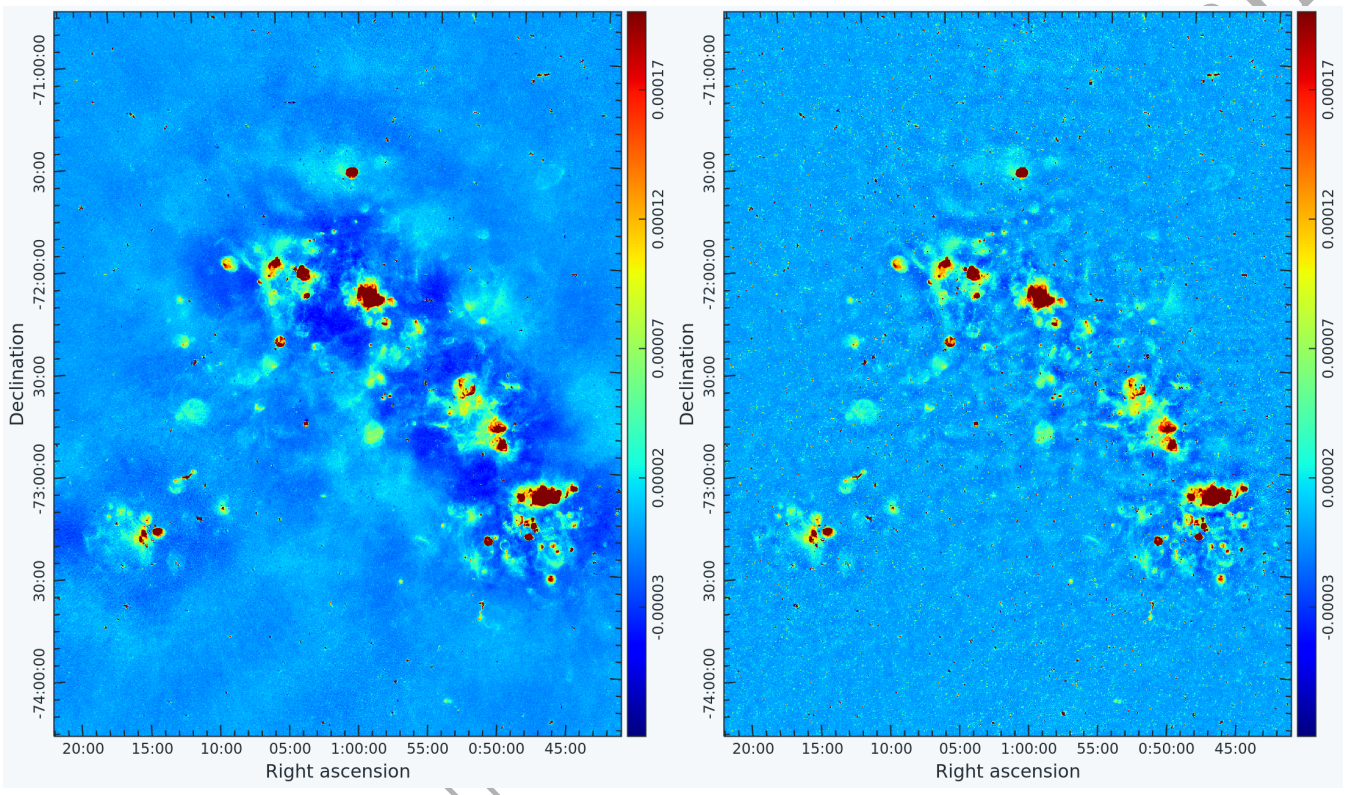

Figure 19. (Left) original (with point sources removed) and (right) background-subtracted or flattened MeerKAT mosaics of the SMC (only showing the central part with diffuse emission on large angular scales). The linear colour scale spans -1×10^{-5} to 2.5×10^{-4} Jy beam^{-1}.

in all 4 images to calculate colour index maps; all of those have large portions of their area with colour index >0.3, and the median colour indices over their full extents are all positive. The five fainter SNRs only have high enough signal-to-noise to calculate indices for a modest number of pixels in their extent, but the median values of those pixels are >0.4 in all cases. Figure 21 shows the colour index map in the south-east SMC, the same region as the 3rd pane of Fig. 14.

To assess the efficacy of the colour index, we examined the 37 regions in the bar and wing of the SMC (the central region shown in Figure 1) with high colour indices that were not already previously identified SNRs, all with median colour indices >0.25. Of these, 26 are compact, clearly background radio galaxies in the MeerKAT image. The remaining 11 include MeerKAT SNR candidates J0049–7322, J0058–7234, J0058–7250, J0112–7304, J0124–7310, the 'mystery object' (see Section 4.6.2.1) and (super)bubble J005119–732408 seen in Fig. 21, the eastern lobe of the nearby (D=293±20 Mpc) radio galaxy MM J01115–7302, QSO PKS 0128–738 (z=2.438), coincidentally in the middle of the S N90 H II region (Henize 1956), and two diffuse regions shown in Fig. 22. We note that the (super)bubble J005119–732408 is 331×291 arcsec^2 (96×86 pc^2) in diameter and shows a low [S II]/Hα ratio of <0.25 indicating that there are no shock excitations as one would find in SNRs. We also checked these two diffuse regions (Fig. 22) and found that they are the most likely part of the wider SMC ISM. Following this blind search, we checked the colour indices of the other five MeerKAT SNR candidates. We found that four were too faint to have calculated the colour index map over their extent, but that

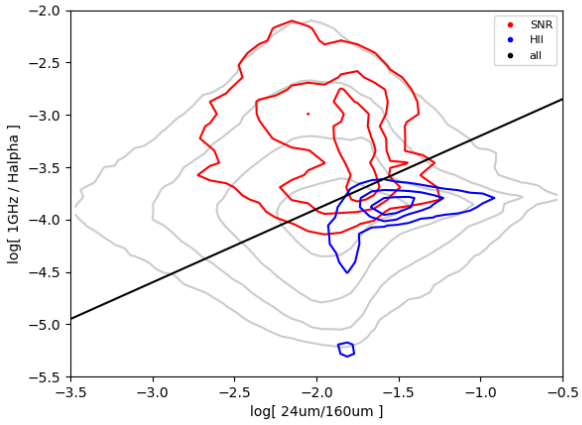

Figure 20. Colour distributions of pixels corresponding to known SMC SNRs (red), known H II regions (blue), and the entire SMC (grey). The best-discriminating line between the known-object training sets, calculated with a support vector machine, is shown. The color index extends from –1.4 to 3.6 for points within the lowest grey contour.

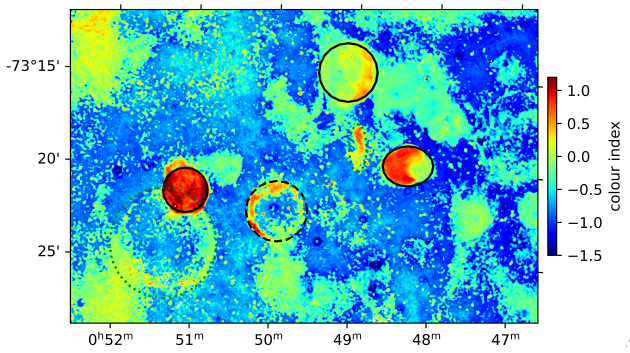

Figure 21. Colour index calculated from centimetre (MeerKAT), Hα, 24 μm and 160 μm images as described in the text. The discriminant was trained to have redder index in known SNRs. Solid ellipses mark three such previously known SNRs. The dashed line marks a new MeerKAT SNR candidate J0049–7322, and dotted lines mark the circularly shaped (super)bubble J005119–732408. The colour index clearly reveals the dashed and dotted sources although it was not trained using those sources.

the few pixels with calculated indices were all high, so consistent with the index measuring non-thermal emission. The final candidate, J0050–7238, happens to have relatively bright diffuse 24 μm and Hα emission coincident with the centre of the SNR, causing a lower colour index, but that emission is morphologically wispier than the rounder SNR candidate, so likely unrelated and merely unfortunately confused along the line of sight.

4.3 MeerKAT SMC pulsar sample

There are 10 known pulsars within the MeerKAT SMC field. Eight of them are SMC pulsars (McConnell et al. 1991; Crawford et al. 2001; Manchester et al. 2006; Titus et al. 2019), including an X-ray magnetar (CXOU J0110043.1−721134, Lamb et al. 2002). The other two are foreground Galactic pulsars: J0057−7201 (Crawford

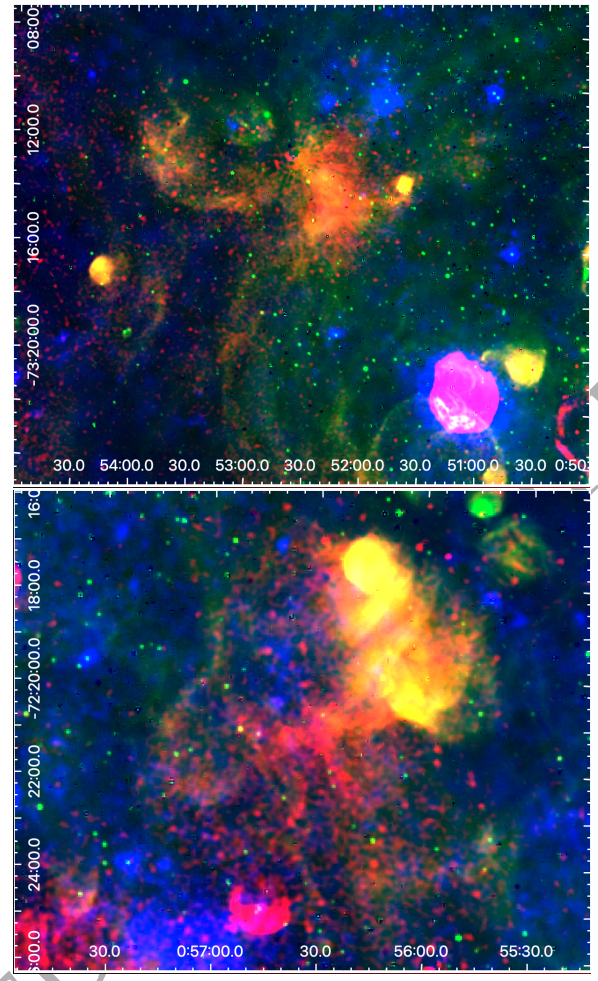

Figure 22. Diffuse regions with high colour index suggestive of potential non-thermal origin. Red, green and blue are the MeerKAT centimetre, MCELS Hα and soft X-ray images. In the top panel, the bright previously known SNR IKT 6 appears towards the bottom right of the field, while in the bottom panel, the SNR candidate J0056–7224 is visible near the bottom, left of center.

et al. 2001) and J0133−6957 (Lyne et al. 1998). In Table 8, we list the parameters of these 10 pulsars obtained from the Australia Telescope National Facility (ATNF) pulsar catalogue (Manchester et al. 2005)[7].

In total, five pulsars were confidently (>5σ) detected by Aegean and we measured their positions and averaged flux densities at 1283.8 MHz (see Table 8). MeerKAT positions and timing positions agree with each other within the uncertainties. For PSR J0057−7201, ours is the first published flux density value at 1.3 GHz. For three relatively bright pulsars, J0045−7319, J0113−7220 and J0133−6957, we were able to measure their flux densities in multiple sub-bands and present the first measurements of their spectral indices. While the spectra of PSRs J0113−7220 and J0133−6957 are consistent with the steep spectrum nature of radio pulsars (e.g., Dai et al. 2015; Murphy et al. 2017; Jankowski et al. 2018), PSR J0045−7319 shows a relatively flat spectrum. Previous MeerKAT pulsar timing-mode observations showed that it is significantly brighter at lower frequencies (Johnston et al. 2020),

[7] http://www.atnf.csiro.au/research/pulsar/psrcat

Table 8. MeerKAT pulsars in the SMC field. The entries for the first four columns are from the ATNF pulsar catalogue. The next four columns are based on MeerKAT data. † is from Kaspi et al. (1994); Bell et al. (1995) and ‡ is from Lamb et al. (2002). The flux limits correspond to a 5σ ($\sim$55 μJy beam^{-1}) no-detection.

Name	RA (J2000) ATNF	Dec (J2000) ATNF	S_{1400} (mJy)	RA (J2000) MeerKAT	Dec (J2000) MeerKAT	Offset (arcsec)	$S_{1283.8}$ (mJy)	α	Notes
J0043−73	00:43:25 (95)	–73:11(7)	0.047				< 0.05		
J0045−7042	00:45:25.69 (17)	–70:42:07.1 (13)	0.11				< 0.1		
J0045−7319	00:45:35.16 (7)	–73:19:03.0 (2)	0.3	00:45:35.2	–73:19:03.3	0.5	0.220	–0.7(2)	Binary†
J0052−72	00:52:28 (95)	–72:05 (7)	0.039				< 0.05		
J0057−7201	00:57:44.0 (4)	–72:01:19 (2)		00:57:44.3	–72:01:18.8	1.3	0.083		Galactic
J0100−7211	01:00:43.03 (11)	–72:11:33.6 (5)					< 0.05		X-ray magnetar‡
J0111−7131	01:11:28.77 (9)	–71:31:46.8 (6)	0.06				< 0.05		
J0113−7220	01:13:11.09 (3)	–72:20:32.20 (15)	0.4	01:13:11.2	–72:20:31.8	0.6	0.300	–1.6(2)	
J0131−7310	01:31:28.51 (3)	–73:10:09.34 (13)	0.15	01:31:28.5	–73:10:09.9	0.5	0.067		
J0133−6957	01:33:32.46 (1)	–69:57:29.68 (3)	0.361	01:33:32.6	–69:57:29.1	0.8	0.530	–2.2(5)	Galactic

suggesting a steep spectrum, and our measurement might be biased by emission related to its binary companion (Kaspi et al. 1994; Bell et al. 1995).

The X-ray magnetar CXOU J0110043.1−721134 in MC-SNR J0100–7211 is not detected and we place a 5σ upper limit of 55 μJy on its radio flux density. However, the SNR associated with this magnetar can be clearly identified (see Fig. 16 top-right) as described in Section 4.1. At the position of two faint pulsars, J0052−72 and J0111−7131, we also identified potential counterparts, but with low significance. The position of PSR J0052−72 is poorly known (Titus et al. 2019) and there are multiple radio sources within its error box of $\sim$ 7 arcmin.

4.4 MeerKAT SMC PNe sample

The proximity of the SMC also allows us to create a sample of radio continuum detected PNe. At the distance of the SMC, we expect that the largest PNe would be a few arcsecs in diameter and therefore a point radio source in our survey. PNe are essential to undertake a variety of studies, e.g. related to the chemical, atomic, molecular and solid-state galactic ISM enrichment (Kwok 2005, 2015; Filipović & Tothill 2021b,a). The MeerKAT survey can detect fainter PNe than previous surveys, helping to build a more complete SMC PNe radio sample.

Previous searches for radio continuum PNe in the SMC (Payne et al. 2008; Filipović et al. 2009; Bojičić et al. 2010; Leverenz et al. 2016; Kavanagh et al. 2019) and recently Asher et al., in prep., yielded 24 PNe detections. Our MeerKAT survey has revealed an additional 19 new PN radio detections (see Table 9), bringing the total number of known SMC PNe detected in various radio surveys to 43 from the sample of 102 optically confirmed (Drašković et al. 2016; Leverenz et al. 2016). We did not detect five previously known radio PNe — they are below the survey's threshold level due to an inverted (optically thick) radio spectrum. The remaining 38 (19 new and 19 previously known) MeerKAT SMC PNe radio detections presented here (Table 9) have been visually inspected and confirmed as true point-source PNe detections.

Table 9. The MeerKAT radio continuum population of PNe in the SMC. In Column 1, with * we indicate 19 new SMC PNe radio detections while in Column 5 we list the separation between the optical position and our radio position determined here. Column 2 abbreviations are from: LHA – Henize (1956), MGPN – Morgan & Good (1985), LIN – Lindsay (1961), [MA93] – Meyssonnier & Azzopardi (1993), [MA95] – Morgan (1995), Jacoby – Jacoby (1980) and SMP – Sanduleak et al. (1978).

Name	PN Name	RA (J2000)	DEC (J2000)	Separation (arcsec)	$S_{1283.8\,\mathrm{MHz}}$ (mJy)	$\alpha \pm \Delta\alpha$
J002359–733804*	LHA 115-N1	00:23:59	–73:38:03.9	0.1	0.084 ± 0.011	—
J002921–721407*	MGPN SMC3	00:29:21	–72:14:07.4	0.8	0.040 ± 0.009	—
J003239–714158	LIN14	00:32:39	–71:41:57.6	2.4	1.513 ± 0.012	–0.12±0.05
J003422–731321	LHA 115-N 4	00:34:22	–73:13:21.5	0.3	0.302 ± 0.009	–0.38±0.20
J004037–732546*	[MA93] 14	00:40:37	–73:25:46.3	0.9	0.092 ± 0.009	—
J004046–751621*	SMP SMC 4	00:40:46	–75:16:21.0	0.2	0.463 ± 0.010	0.04±0.12
J004122–724517	LHA 115-N 5	00:41:22	–72:45:17.0	0.2	0.713 ± 0.009	0.21±0.08
J004127–750251*	MGPN SMC 5	00:41:27	–75:02:51.2	0.5	0.067 ± 0.008	—
J004228–732055*	Jacoby SMC 1	00:42:28	–73:20:55.2	0.2	0.160 ± 0.010	–0.22±0.28
J004309–730804*	[MA93] 44	00:43:09	–73:08:04.5	0.9	0.065 ± 0.011	—
J004325–723819	LIN 43	00:43:25	–72:38:19.0	0.2	0.542 ± 0.009	0.18±0.07
J004426–735139*	MGPN SMC 6	00:44:26	–73:51:39.4	0.2	0.070 ± 0.007	—
J004521–732411	LIN 66	00:45:21	–73:24:10.9	0.9	0.221 ± 0.012	–1.00±0.16
J004528–734215*	LIN71	00:45:28	–73:42:15.1	0.7	0.097 ± 0.007	—
J004700–724917	LHA 115-N 18	00:47:00	–72:49:16.6	0.2	0.369 ± 0.007	–0.20±0.09
J004921–735258*	[MA93] 291	00:49:21	–73:52:58.4	0.2	0.117 ± 0.007	—
J004952–734421	LIN 144	00:49:52	–73:44:21.4	0.3	0.600 ± 0.008	1.03±0.06
J005035–734258	LIN 134	00:50:35	–73:42:58.1	0.2	0.452 ± 0.007	–0.08±0.09
J005107–735738	LIN 174	00:51:07	–73:57:37.7	0.9	0.298 ± 0.008	1.01±0.17
J005156–712444	LIN 191	00:51:56	–71:24:44.4	0.2	0.917 ± 0.011	0.57±0.05
J005311–724507	Jacoby SMC 20	00:53:11	–72:45:07.7	0.2	0.509 ± 0.014	0.19±0.05
J005343–733707*	[MA93]700	00:53:43	–73:37:06.9	0.2	0.074 ± 0.009	—
J005605–701926*	LHA 115-N 54	00:56:05	–70:19:25.6	1.2	0.088 ± 0.008	—
J005620–720658	LIN 302	00:56:19	–72:06:58.4	1.0	0.211 ± 0.010	–0.53±0.31
J005631–722702	[MA93]943	00:56:31	–72:27:02.3	0.4	0.334 ± 0.010	1.00±0.23
J005723–724817*	[MA93]999	00:57:23	–72:48:17.6	1.2	0.065 ± 0.012	—
J005837–713549	LIN 333	00:58:37	–71:35:49.1	0.4	0.541 ± 0.009	–0.15±0.10
J005842–725700	Jacoby SMC 26	00:58:42	–72:57:00.0	0.5	0.278 ± 0.010	–0.47±0.16
J005916–720200	LIN 347	00:59:16	–72:02:00.0	0.3	0.573 ± 0.012	0.49±0.09
J005940–713815*	LIN 357	00:59:40	–71:38:15.4	1.0	0.066 ± 0.018	—
J010418–732151	LIN 430	01:04:18	–73:21:51.3	0.5	0.165 ± 0.008	–0.48±0.22
J010451–730522*	MGPN SMC 10	01:04:51	–73:05:21.6	1.2	0.098 ± 0.011	—
J011211–712651*	[MA93] 1757	01:12:11	–71:26:51.1	1.1	0.121 ± 0.012	—
J011240–725347*	[MA93] 1762	01:12:40	–72:53:47.0	0.4	0.074 ± 0.010	—
J011424–710521*	MGPN SMC 12	01:14:24	–71:05:20.9	0.3	0.138 ± 0.011	—
J012111–731435	LHA 115-N 87	01:21:11	–73:14:34.8	0.1	0.836 ± 0.010	0.42±0.09
J012412–740232	LIN536	01:24:12	–74:02:32.0	0.4	0.283 ± 0.010	0.67±0.23
J012440–713727*	[M95]8	01:24:40	–71:37:27.0	0.2	0.067 ± 0.010	—

The results for these 38 SMC PNe are presented in Table 9 which includes PNe other names, position, separation between optical and radio position, flux density, and spectral index (where possible) based on the MeerKAT in-band measured flux densities. The average separation between our radio sources and corresponding previously established optical detections is 0.55 arcsec with SD of 0.13 arcsec, indicating that the majority of these correspond to true PNe detections. However, PNe LIN14 has a significantly larger separation (2.4 arcsec), and being the strongest radio source in this sample (1.5 mJy) might indicate a possible different nature as examined in Filipović et al. (2009). Most of the SMC PNe have typical radio continuum spectra (–0.5< α <+1.0; Filipović et al. 2009; Bojičić et al. 2021) and their flux densities are in agreement with previous measurements at similar frequencies where those exist. A more in-depth study of the entire SMC PNe sample will be presented elsewhere (Asher et al., in prep.).

4.5 Radio stars in the SMC field

We have searched for radio stars in the field of view of the MeerKAT image, comprising both thin and thick disk populations from our Galaxy and stars in the SMC. As noted before, our point source catalogue contains 108,330 sources, and we cross-matched this with SIMBAD (Wenger et al. 2000) and GAIA DR3 (Gaia Collaboration et al. 2016, 2022). Due to the nature of the field, the GAIA catalogue is extremely crowded, making the cross-matching process difficult, with a high number of spurious matchings, calculated by shifting the MeerKAT source catalogue by 0.1 degree and matching it with the GAIA one. To find a compromise between having a good number of matches and not having too many spurious matches, we analysed the spurious match percentage p and the number of new sources $N_{\rm new}$ at different matching radii. In the following, N_{r_i} and S_{r_i} are the number of matches and spurious matches, respectively, that we obtain using r_i as our matching radius, where we step through radii in bins of 0.05 arcsec:

$$N_{\rm new} = (N_{r_i} - S_{r_i}) - (N_{r_{i-1}} - S_{r_{i-1}}); \quad (3)$$

$$p = 100 * S_{r_i}/N_{r_i}. \quad (4)$$

As can be seen in Fig. 23, p increases with matching radius while $N_{\rm new}$ tends to decrease. A good compromise can be found at r=0.6 arcsec, where $N_{\rm new}$ has a local maximum of $N_{\rm new} \approx 200$ and $p \lesssim 30$ per cent. At r=0.6 arcsec we found 3777 matches, with $\sim$ 1000 expected to be spurious. GAIA DR3 supplies several parameters for each source, in particular three of great relevance here: $p_{\rm star}$, $p_{\rm galaxy}$ and $p_{\rm quasar}$, the probability, knowing all the other parameters about that particular source, of the source being a star, a galaxy or a quasar, respectively (Creevey et al. 2022). It is important to note that the compact MeerKAT SMC catalogue sources suffer from the strong bias of being $\sim$ 1 GHz radio sources, meaning that their probability of being a galaxy is higher than the typical GAIA source. To check the reliability of these parameters we matched the MeerKAT sources with SIMBAD, finding 415 matches within a 1 arcsec radius that also have a GAIA match. Among them, 101 sources have $p_{\rm star} > 0.99$ in GAIA but 29 are classified as being galaxies in SIMBAD. It is therefore clear that this parameter alone cannot be used to discriminate between radio stars and galaxies.

To create catalogues of radio star candidates we proceeded on two parallel tracks: exploiting the proper motion parameter and using the SIMBAD catalogue to isolate known stars. Proper motion is a constraining parameter, whereby nearly all sources with a measured proper motion should be stars. Among all the sources in the MeerKAT catalogue, there are just 141 with a measured proper motion $\mu > 5$ mas year^{-1}, 85 per cent of which are classified with the $p_{\rm star}$ parameter; 91 of them have $p_{\rm star} > 0.99$. Using a more stringent cut of $\mu > 10$ mas year^{-1}, we find 32 sources, 26 with the $p_{\rm star}$ parameter, and 24 with $p_{\rm star} > 0.99$.

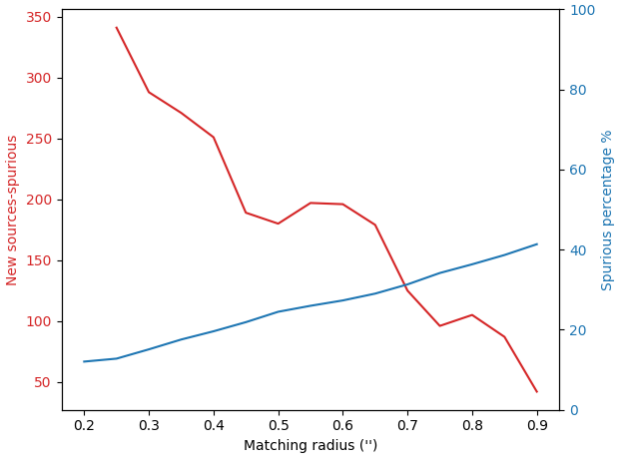

Figure 23. Plot of $N_{\rm new}$ (in red) and the spurious percentage p (in blue) as a function of the matching radius. p increases with matching radius, while $N_{\rm new}$ decreases, with a possible plateau around 0.6 arcsec.

We assemble a "golden sample" of radio stars from these 24 sources plus another 5 sources with a measured proper motion $\mu > 5$ mas year^{-1} and classified as stars by SIMBAD. These 29 sources are listed in Table 10. With fewer restrictions (e.g., on proper motion cuts) one can assemble different samples that capture a larger numbers of stellar objects, including YSOs, red giant branch candidate, and RR Lyrae, even if at the cost of larger cross-contamination. That work will be presented elsewhere.

To compare the 29 stars in our golden sample with expectations from the literature, we considered the work of Yu et al. (2021). Using their scaling relations for a detection threshold of $\sim$ 20μJy (the faintest detection in our MeerKAT catalogue), and considering only M stars (our SMC field is away from the Galactic Plane, and at this sensitivity M stars should be closer than $\sim$ 200 pc and distributed approximately isotropically, unlike some other stellar populations), we expect that $\sim$ 80 M stars might be detected across our 7°×7° field. Given this very rough extrapolation, and considering that there are more stars detected in our field of view once the stringent constraints of the golden sample are relaxed, the detection rate is compatible with expectations. Considering that only $\sim$ 1000 radio stars have been identified to date (see Güdel 2002), the likely identification of $\sim$ 100 new ones in the small field of view of our SMC survey points to the ability of high sensitivity and resolution surveys such as this one to significantly advance the study of radio stars.

4.6 Individual sources of interest

We also show other interesting sources found in these MeerKAT SMC images. They encompass various foreground and background sources such as stars and AGN.

4.6.1 Circularly polarised point sources

We use our new MeerKAT Stokes V image of the SMC field to search for circularly polarised sources. Applying a cut-off |V/I| in-

Table 10. Golden sample of candidate radio stars, selected as described in Section 4.5.

Name	RA (J2000)	DEC (J2000)	GAIA designation	pm (mas yr^{-1})	$p_{\rm star}$	SIMBAD main_type
J004231–741155	00:42:31.07	–74:11:55.0	Gaia DR3 4685749263432487040	5.96	0.99992	Star
J004403–743734	00:44:03.49	–74:37:34.0	Gaia DR3 4685490259707560832	31.4	0.9998	RotV*
J005205–744649	00:52:04.85	–74:46:49.3	Gaia DR3 4684816740118487936	32.8	0.9988	Star
J005325–710243	00:53:25.46	–71:02:42.7	Gaia DR3 4689370676764568576	37.4	0.9998	Star
J005611–724749	00:56:10.82	–72:47:49.2	Gaia DR3 4685980435808569344	5.89	0.000004	Star
J010314–705059	01:03:14.46	–70:50:59.0	Gaia DR3 4690839693019667840	6.83	-	Star
J011322–724520	01:13:21.92	–72:45:20.4	Gaia DR3 4687241365113885440	20.5	0.9997	Star
J011517–731143	01:15:16.56	–73:11:43.2	Gaia DR3 4687166877510636032	31.1	-	Star
J011705–722844	01:17:04.72	–72:28:44.2	Gaia DR3 4687350732164591104	6.54	0.99991	Star
J011710–702150	01:17:09.72	–70:21:49.7	Gaia DR3 4690959294964458880	33.2	0.9997	Star
J012711–701022	01:27:10.58	–70:10:22.5	Gaia DR3 4691120446431145088	10.3	0.999991	Cepheid
J002741–744049	00:27:41.09	–74:40:48.9	Gaia DR3 4685345467763983104	16.5	0.99998	-
J003329–713246	00:33:29.25	–71:32:46.1	Gaia DR3 4690033750987052800	52.0	0.99994	-
J004627–734621	00:46:27.07	–73:46:20.9	Gaia DR3 4685776265879398656	10.9	0.9998	-
J004733–731701	00:47:33.22	–73:17:01.0	Gaia DR3 4685942708820468224	12.8	0.997	-
J004752–732455	00:47:52.47	–73:24:54.9	Gaia DR3 4685926422305317504	10.1	0.9997	-
J005445–745554	00:54:45.49	–74:55:53.9	Gaia DR3 4684753312040026112	38.8	0.996	-
J005621–730647	00:56:20.66	–73:06:46.6	Gaia DR3 4685912815770474368	13.0	0.995	-
J005759–723741	00:57:59.21	–72:37:40.8	Gaia DR3 4685988613398832000	21.2	0.99997	-
J005815–744629	00:58:14.85	–74:46:29.0	Gaia DR3 4684760561944723456	29.4	0.99991	-
J010338–732726	01:03:38.34	–73:27:25.8	Gaia DR3 4685691573434514176	10.2	0.994	-
J010631–714838	01:06:31.12	–71:48:38.5	Gaia DR3 4690540282257021440	10.9	0.99992	-
J010711–753224	01:07:11.07	–75:32:24.1	Gaia DR3 4684485198699244672	30.0	0.99988	-
J010746–704641	01:07:45.88	–70:46:41.0	Gaia DR3 4690832683625105152	12.4	0.99997	-
J011249–701317	01:12:48.53	–70:13:17.0	Gaia DR3 4690956138162512256	20.5	0.99995	-
J012221–714122	01:22:20.77	–71:41:22.2	Gaia DR3 4687587337618874240	18.4	0.99997	-
J012740–734651	01:27:39.77	–73:46:50.6	Gaia DR3 4686223290360321664	36.2	0.99998	-
J013527–725507	01:35:27.13	–72:55:07.5	Gaia DR3 4686843586718702464	24.4	0.999992	-
J014028–702341	01:40:27.60	–70:23:41.0	Gaia DR3 4688123860632580352	10.1	0.9998	-

tensity of >1 per cent we found 11 sources (Table 11) from which the brightest (|V/I|) two are nearby stars (ISO-MCMS J010037.4–730036 and HFP2000 665; Haberl et al. 2000; Sturm et al. 2013a) at a distance of D=81 pc and 86 pc (Fig. 24). Another source found in this study is the well-known nearby radio star V* CF Tuc (Budding et al. 1999) at D=87 pc, an RS CVn type binary (Fig. 24, left). These three and J013117−730356 (4XMM J013117.0−730356) are detected in X-rays (see below). Using VizieR we found no counterpart at other wavelengths within 3 arcsec for three sources (J002208–712355, J005244–755103, and J011549–755652), while all others are detected at infrared wavebands by *Spitzer* and *WISE* (CatWISE2020 catalogue; Marocco et al. 2021).

The peak flux density for these 11 sources ranges over 2.5 orders of magnitude: 0.06–14 mJy beam^{-1}. Similarly, the spectral index is also widely distributed. Source J005243−755102 displays a nominally very steep spectrum with $\alpha = -1.47 \pm 0.73$, although the uncertainty is very large despite 12 sub-band flux density measurements. At face value it is challenging to physically interpret this in terms of an incoherent emission mechanism.

In addition to being a highly circularly polarised source, ISO-MCMS J010037.4–730036 is a variable object. There were seven images from our MeerKAT survey including its position; three observations done on the same day all showed bright I and V emission but with none of the artefacts seen that are characteristic of rapidly variable sources. None of the other four observations (two on the same day but different from those in which signals were detected) showed detectable emission in I or V. Hence, the time scale on which substantial variability occurs is of order a day. It is unlikely that J010037.4–730036 is a flare star – the variability time scale is too long. It may be an RS CVn-type binary, which are known to produce highly circularly polarised emission at decimetre wavelengths that are polarised in the opposite sense of higher-frequency emissions. This has been interpreted in terms of plasma radiation (e.g., White & Franciosini 1995, and references therein). However, the degree of polarisation is typically less (< 50 per cent) than that observed on J010037.4–73003. A more likely possibility is that this source is a late-type dwarf and auroral emitter by means of the cyclotron maser instability (e.g., Treumann 2006). A recent example of this class of radio emitter is the dM5.5 star UV Cet discussed by Bastian et al. (2022) which produces flux density similar in I and V when scaled to the appropriate distance.

Three of the circularly polarised objects in Table 11 have been observed in X-rays. ISO-MCMS J010037.4–730036 was serendipitously observed since 1979 more than 35 times with various X-ray observatories and shows long-term X-ray variability of at least a factor of five (Sturm et al. 2013a). Source J005445−745554 (a.k.a. [HFP2000] 665) was detected in a deep (50 ks) *ROSAT* pointed observation in October 1992, but no variability information is available. Finally, for source J013117−730356 we identify 4XMM J013117.0−730356 as its X-ray counterpart (4XMM-DR11 catalogue; Webb et al. 2020). *XMM–Newton* observed the source twice in 2016 with one detection at $(7.9\pm0.9) \times 10^{-15}$ erg s^{-1} cm^{-2}. During an *Einstein* observation in 1979 the source was a factor of ∼80 brighter than during the *XMM–Newton* observation. The X-ray detections and in particular the variability support the picture of stars with a highly active corona.

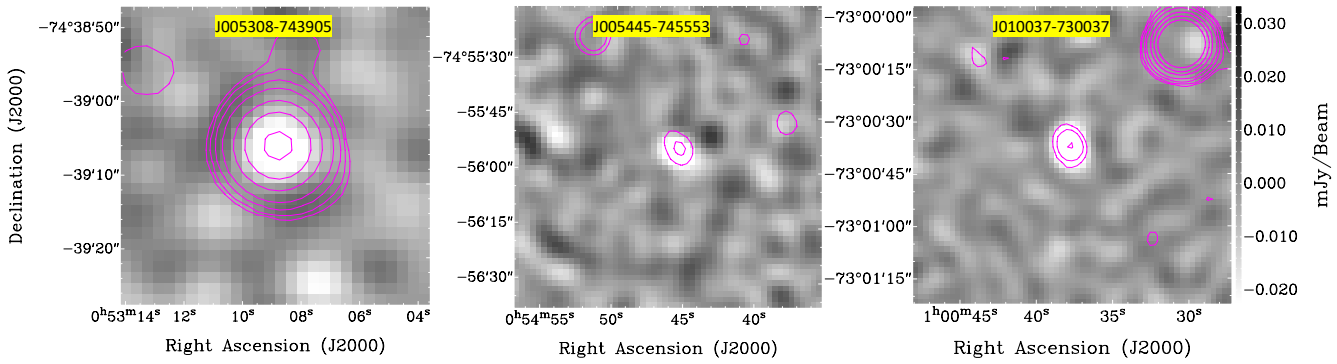

Figure 24. Three circularly polarised nearby stars in the field of the SMC: V* CF Tuc (left), [HFP2000] 665 (middle) and ISO-MCMS J010037.4–730036 (right). Greyscale is from Stokes V image while contours (3σ, 5σ, 10σ, 20σ, 50σ, 100σ and 200σ) are from Stokes I image.

Table 11. MeerKAT Stokes V point sources in the SMC field. The source positions (RA and Dec) are from the V image. In Column 5 we list the source peak flux density at MeerKAT broad-band frequency of 1283.8 MHz.

No.	Name	RA (J2000)	Dec (J2000)	S_p (mJy beam^{-1})	|V/I| (%)	$\alpha \pm \Delta\alpha$	Notes
1	J002208–712355	00:22:08.5	–71:23:55.5	0.169	24.5	–1.15±0.21	
2	J005244–755103	00:52:43.7	–75:51:02.7	1.021	7.1	–1.47±0.72	
3	J005309–743905	00:53:08.9	–74:39:05.9	2.333	1.7	+0.04±0.02	V* CF Tuc; Budding et al. (1999)
4	J005445–745554	00:54:45.5	–74:55:53.9	0.059	80.8	—	X-rays: HFP2000 665; Haberl et al. (2000)
5	J005507–701749	00:55:07.3	–70:17:48.5	2.984	1.3	–0.12±0.03	
6	J010038–730037	01:00:37.7	–73:00:37.0	0.103	70.3	—	ISO-MCMS J010037.4–730036 Sturm et al. (2013a)
7	J011549–755652	01:15:49.2	–75:56:57.1	14.193	1.03	+0.56±0.03	
8	J012921–724944	01:29:21.0	–72:49:44.1	0.064	49.7	—	
9	J013117–730356	01:31:17.1	–73:03:55.9	4.125	1.0	–0.13±0.01	X-rays: 4XMM J013117.0−730356; Webb et al. (2020)
10	J013601–725059	01:36:01.2	–72:50:59.0	7.024	1.1	–0.32±0.07	
11	J013635–744331	01:36:35.2	–74:43:30.7	4.030	1.3	–0.66±0.09	

4.6.2 Extended sources

There are a large number of extended sources with various morphologies that we catalogued as BCE (Section 3.1.1 and Table 5). Many, but not all of these, are background objects such as AGN and star-forming galaxies. Here we introduce a small sample of interesting objects selected from the BCE list.

4.6.2.1 Non-thermal filaments in the southern part of the SMC

In Figs. 14 (marked with '?') and 25, we point to an interesting extended feature of size ~100 arcsec (29 pc at the distance to the SMC) and position just south from the N19 region. We cannot associate this feature with any specific source type. Specifically, we investigated possible SNR or AGN nature but the morphology of this object is different. It is also exclusively seen in radio continuum frequencies suggesting non-thermal origin. Its elongated shape and vicinity to other well-known SMC sources indicate possible SMC membership. However, it is somewhat similar to bent and twisted radio continuum jets around the peculiar galaxy pair ESO 295-IG022 (Read et al. 2001; Filipovic et al. 2010). It also coincides with an AGN candidate seen in the VISTA Magellanic Clouds (VMC) Survey (Cioni et al. 2011, and reference therein) image (red, probably fairly high redshift). There is a faint AGN candidate at RA(J2000)=$00^h48^m56^s$ and Dec(J2000)=–73°18′34″which has a position consistent with being the central source of the radio jets/lobes. Most interestingly, Carli et al. (in prep.) report a young pulsar at RA(J2000)=$00^h48^m56^s$ and Dec(J2000)=–73°17′44" (with 2 arcsec positional error) that is ~5 arcsec from the radio point-like source J004857–731747 located at the northern tip of this feature (see Fig. 25). As seen in the case of the DEM S5 SNR, the pulsar and radio continuum emission could be slightly displaced and still be related if the latter includes emission from a PWN. The radio feature could be a bow-shock PWN with the emission south of the pulsar representing the tail and the radio point source as the PWN "head". There is no obvious nearby SNR that could be associated with such a putative PWN, but that would not be exceptional — several Galactic bow-shock PWNe have no parent SNR, such as for example the "Potoroo" PWN (Lazarević et al. submitted). We tentatively classify this source as a PWN, but further study is required to establish its nature.

4.6.2.2 Radio ring galaxy ESO 029–G034

Among the most interesting of the extragalactic discoveries in this survey is the radio ring galaxy (RaRiGx) ESO 029–G034 at a distance of 155 Mpc (z=0.036) and diameter of ~65 kpc. This could be a new type of object. As an optical source, it is classified as an interacting double and the largest in the group (Arp & Madore 1987). However, in the VMC Survey optical images, we can clearly see a face-on spiral galaxy with the dominant optical bar and bulge in the centre. Interestingly, its radio continuum emission is anti-correlated with optical emission as can be seen in Fig. 26. Also, Elias-Rosa et al.

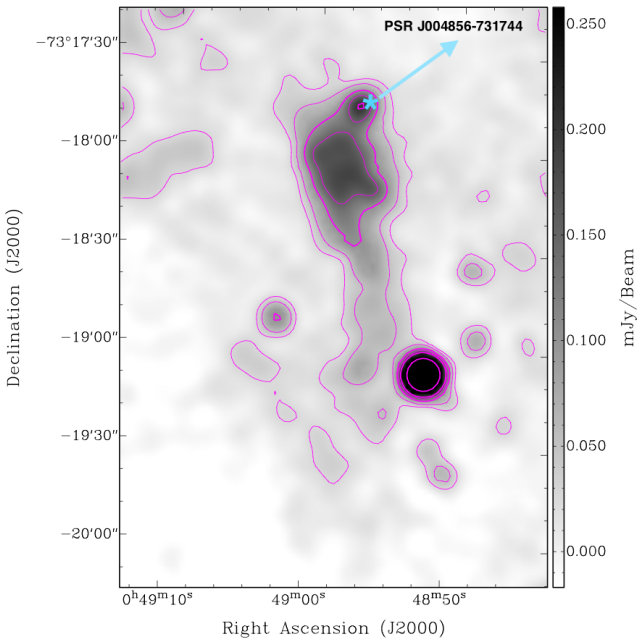

Figure 25. MeerKAT image of the unknown non-thermal feature (also marked with '?' in Fig. 14). The contours are 0.025, 0.05, 0.1, 0.15, 0.2 and 0.5 mJy beam^{-1}. The light blue star marks the position of pulsar J004856–731744 (Carli et al. (in prep.)).

(2014)[8] reported the detection of Supernova (SN) OGLE-2014-SN-046 at RA(J2000)=01^{h}09^{m}06.73^s and Dec(J2000)=–74°30′46.4″. A point-like optical source linked to this Type-IIP SN is located on the radio ring (see Fig. 26).

4.6.2.3 Nearby spirals As in other modern radio surveys (e.g., see Knowles et al. 2022), continuum emission is detected in our survey from nearby face-on spiral galaxies. In Fig. 27 we show three such visually striking objects: 2MASX J01215707–7516248, ESO 029–G047 and ESO 029–G049 at distances of 99 Mpc, 300 Mpc and 174 Mpc, respectively. We measure their spectral index as –0.11±0.10, –0.23±0.10 and –0.29±0.10, respectively, indicating that thermal emission dominates across these spiral galaxies.

5 SUMMARY AND CONCLUSIONS

We have imaged the SMC at 0.9–1.7 GHz using the MeerKAT radio telescope with a median Stokes I rms of ~11 μJy beam^{-1}. A variety of products are included in the data release associated with this paper. These include a catalogue of point and compact extended radio continuum sources across a ~7°×7° FoV. The catalogue consists of 108,330 point sources and 517 compact extended sources above 5× local rms in the broad-band image (a.k.a. channel 0 or total intensity/full band; frequency ν=1283.8 MHz; bandwidth of 800 MHz; beam size of 8 arcsec). The vast majority of catalogued point radio sources are unrelated to the SMC, with only a small number of intrinsic PNe, compact H II regions and YSOs as well as foreground stars. However, we expect that about 50 per cent of 517 bright compact extended sources are extragalactic objects such as AGN with clearly visible radio jets while others could be intrinsic SMC objects such as complex H II regions. We report each source position (RA, Dec and errors), peak flux densities (with corresponding local rms noise), integrated flux densities (with corresponding errors), and spectral index values that we judge to be reliable for a subset of the sources.

We used our imaging products to investigate the population of SMC SNRs, pulsars, and PNe, while also considering some foreground and background objects. Our main results include:

(i) Detection of all previously established SMC SNRs and SNR candidates; identification of 10 new SNR candidates; confirmation of MCSNR J0100–7211 as a bona fide SNR with the X-ray magnetar CXOU J0110043.1−721134 at its centre;
(ii) Firm detection of five radio pulsars and two weak radio sources potentially associated with known pulsars, out of 10 known pulsars in the FoV. An X-ray magnetar is not detected as a radio source but is found to be in the centre of a newly established SNR;
(iii) Detection of 38 out of 102 optically known PNe, of which half are new detections. Almost all of them have a typical PNe spectrum but a few such as SMP 9 (LIN66) unexpectedly show a steep spectrum;
(iv) Detection of three nearby radio stars at a distance of ~80 pc, among a total of 11 sources that are circularly polarised;
(v) A number of interesting background objects, of which RaRiGx ESO 029–G034 at a distance of 155 Mpc and diameter of ~65 kpc might represent a new type of radio object.

ACKNOWLEDGEMENTS

The MeerKAT telescope is operated by the South African Radio Astronomy Observatory, which is a facility of the National Research Foundation, an agency of the Department of Science and Innovation. The National Radio Astronomy Observatory is a facility of the National Science Foundation, operated under a cooperative agreement by Associated Universities, Inc.

DATA AVAILABILITY

Raw visibility data is available from the SARAO archive (https://archive.sarao.ac.za/) under project codes SSV-20190715-FC-02 and SSV-20200131-SP-01. Image data products are available using DOI https://doi.org/10.48479/1fdb-r233. The L-band mosaic FITS images are as described in Cotton (2019). The mosaics in Stokes I, Q, U and V are 7.08° × 7.08° with 1.5 arcsec pixels centred at J2000 position RA=01:00:0.0 and Dec=–73:00:00.0. The mosaic cubes contain 16 planes. The first plane is the band-weighted average flux density at the effective frequency of 1310.89 MHz, the second plane (Stokes I only) is the fitted spectral index or blanked if no fit could be made, planes 3–16 are the frequency bins centred at the frequencies given in Table 3. Two planes are totally blanked due to RFI. The second plane of the Q, U and V images are not physically meaningful and are blanked. For Stokes I, a second cube is provided in which the first plane is the broad-band flux density, the second plane is the spectral index where fitted, the third plane is the least squares error estimate for the intensity, the fourth plane is the error estimate for spectral index and the fifth plane the χ^2 of the fit. For Stokes Q, U and V, single-plane images of the broad-band average are provided. A single pointing image at UHF band (544–1088 MHz) with effective frequency of 870.0 MHz is centred at RA=00:52:44.0, dec=-72:49:42 and is 5.0°×5.0°

[8] Also see `http://ogle.astrouw.edu.pl/ogle4/transients/2014/transients.html`.

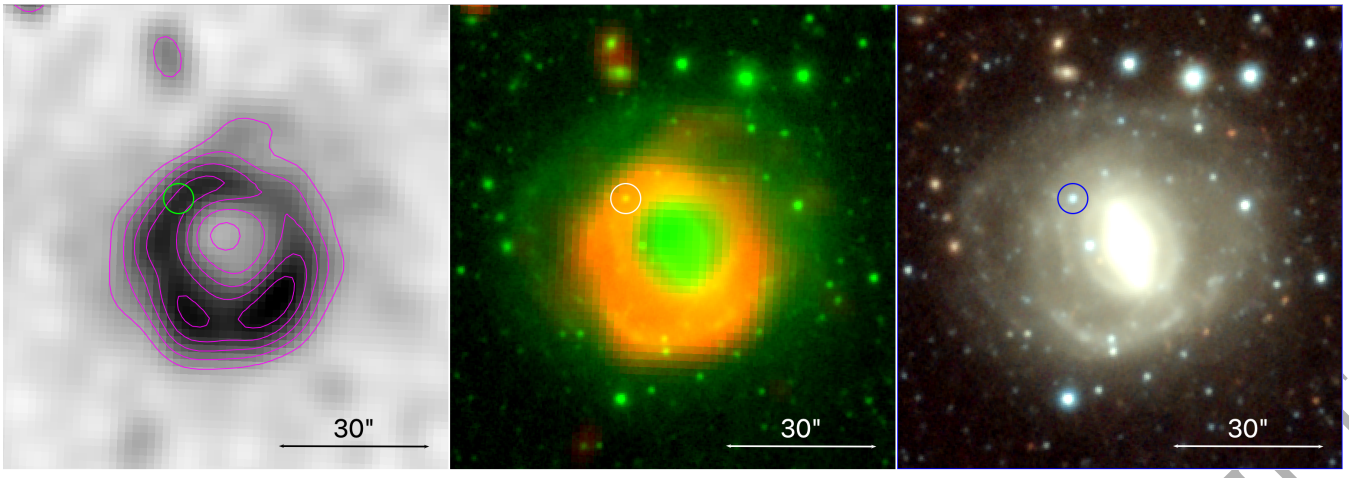

Figure 26. Spiral galaxy ESO 029–G034 (a.k.a. karakondžula) where left is MeerKAT image with contours of 50, 75, 100, 125 and 150 μJy beam^{-1}, the middle image is a red-green mix from VMC Ks band and MeerKAT (red). On the right is VMC Ks, J and Y bands composite RGB image where the north is up. The circles in each panel indicate the position of SN OGLE-2014-SN-046.

in extent. The catalogues underlying this article are available on the CDS/VizieR (`https://cds.u-strasbg.fr/`) website as well as from the SARAO archive (https://archive.sarao.ac.za/). The full point and compact extended source catalogues (Tables 4 and 5) are also provided through the CDS/VizieR service.

REFERENCES

Alsaberi R. Z. E., et al., 2019, MNRAS, 486, 2507
Arp H. C., Madore B., 1987, A catalogue of southern peculiar galaxies and associations. Cambridge ; New York : Cambridge University Press
Bastian T. S., Cotton W. D., Hallinan G., 2022, ApJ, 935, 99
Bell J. F., Bessell M. S., Stappers B. W., Bailes M., Kaspi V. M., 1995, ApJ, 447, L117
Bojičić I. S., Filipović M. D., Crawford E. J., 2010, Serbian Astronomical Journal, 181, 63
Bojičić I. S., Filipović M. D., Urošević D., Parker Q. A., Galvin T. J., 2021, MNRAS, 503, 2887
Bozzetto L. M., et al., 2017, ApJS, 230, 2
Bozzetto L. M., et al., 2023, MNRAS, 518, 2574
Broadbent A., Haslam C. G. T., Osborne J. I., 1989, MNRAS, 237, 381
Brunthaler A., et al., 2021, A&A, 651, A85
Budding E., Jones K. L., Slee O. B., Watson L., 1999, MNRAS, 305, 966
Camilo F., Scholz P., Serylak M., et al. 2018, ApJ, 856, 180
Carli E., et al., 2022, MNRAS, 517, 5406
Cioni M. R. L., et al., 2011, A&A, 527, A116
Clarke J. N., 1976, MNRAS, 174, 393
Cohen M., et al., 2007, MNRAS, 374, 979
Collier J. D., et al., 2018, MNRAS, 477, 578
Cotton W. D., 2008, PASP, 120, 439
Cotton W. D., 2017, PASP, 129, 094501
Cotton W. D., 2019, Obit Memo series, 63, 1
Cotton W. D., et al., 2018, ApJ, 856, 67
Cotton W. D., et al., 2020, MNRAS, 495, 1271
Crawford F., Kaspi V. M., Manchester R. N., Lyne A. G., Camilo F., D'Amico N., 2001, ApJ, 553, 367
Crawford E. J., Filipović M. D., de Horta A. Y., Wong G. F., Tothill N. F. H., Draskovic D., Collier J. D., Galvin T. J., 2011, Serbian Astronomical Journal, 183, 95
Crawford E. J., Filipović M. D., McEntaffer R. L., Brantseg T., Heitritter K., Roper Q., Haberl F., Urošević D., 2014, AJ, 148, 99
Creevey O. L., et al., 2022, arXiv e-prints, p. arXiv:2206.05864
Dai S., et al., 2015, MNRAS, 449, 3223
Davies R. D., Elliott K. H., Meaburn J., 1976, Mem. RAS, 81, 89
Dempsey J., et al., 2022, Publ. Astron. Soc. Australia, 39, e034
Drašković D., Parker Q. A., Reid W. A., Stupar M., 2016, in Journal of Physics Conference Series. p. 072008 (`arXiv:1603.07955`), doi:10.1088/1742-6596/728/7/072008
Elias-Rosa N., et al., 2014, The Astronomer's Telegram, 6399, 1
Esposito P., Rea N., Israel G. L., 2021, in Belloni T. M., Méndez M., Zhang C., eds, Astrophysics and Space Science Library Vol. 461, Astrophysics and Space Science Library. pp 97–142 (`arXiv:1803.05716`), doi:10.1007/978-3-662-62110-3_3
Filipović M. D., Tothill N. F. H., eds, 2021a, Multimessenger Astronomy in Practice. 2514-3433, IOP Publishing, doi:10.1088/2514-3433/ac2256, `https://dx.doi.org/10.1088/2514-3433/ac2256`
Filipović M. D., Tothill N. F. H., 2021b, Principles of Multimessenger Astronomy. 2514-3433, IOP Publishing, doi:10.1088/2514-3433/ac087e, `https://dx.doi.org/10.1088/2514-3433/ac087e`
Filipovic M. D., White G. L., Jones P. A., Haynes R. F., Pietsch W. N., Wielebinski R., Klein U., 1996, in Burkert A., Hartmann D. H., Majewski S. A., eds, Astronomical Society of the Pacific Conference Series Vol. 112, The History of the Milky Way and Its Satellite System. p. 91
Filipović M. D., Jones P. A., White G. L., Haynes R. F., Klein U., Wielebinski R., 1997, A&AS, 121, 321
Filipović M. D., Haynes R. F., White G. L., Jones P. A., 1998, A&AS, 130, 421
Filipović M. D., Haberl F., Pietsch W., Morgan D. H., 2000, A&A, 353, 129
Filipović M. D., Bohlsen T., Reid W., Staveley-Smith L., Jones P. A., Nohejl K., Goldstein G., 2002, MNRAS, 335, 1085
Filipović M. D., Payne J. L., Reid W., Danforth C. W., Staveley-Smith L., Jones P. A., White G. L., 2005, MNRAS, 364, 217
Filipović M. D., et al., 2008, A&A, 485, 63
Filipović M. D., et al., 2009, MNRAS, 399, 769
Filipovic M. D., Crawford E. J., Jones P. A., White G. L., 2010, Serbian Astronomical Journal, 181, 31
Filipović M. D., et al., 2021, MNRAS, 507, 2885
Filipović M. D., et al., 2022, MNRAS, 512, 265
Filipović M. D., et al., 2023, AJ, 166, 149
Findlay J. W., 1966, ARA&A, 4, 77
Flesch E. W., 2021, arXiv e-prints, p. arXiv:2105.12985
For B.-Q., et al., 2018, MNRAS, 480, 2743
Gaia Collaboration et al., 2016, A&A, 595, A2
Gaia Collaboration et al., 2022, arXiv e-prints, p. arXiv:2208.00211
Galvin T. J., Filipovic M. D., 2014, Serbian Astronomical Journal, 189, 15
Gordon K. D., et al., 2009, ApJ, 690, L76
Graczyk D., et al., 2020, ApJ, 904, 13

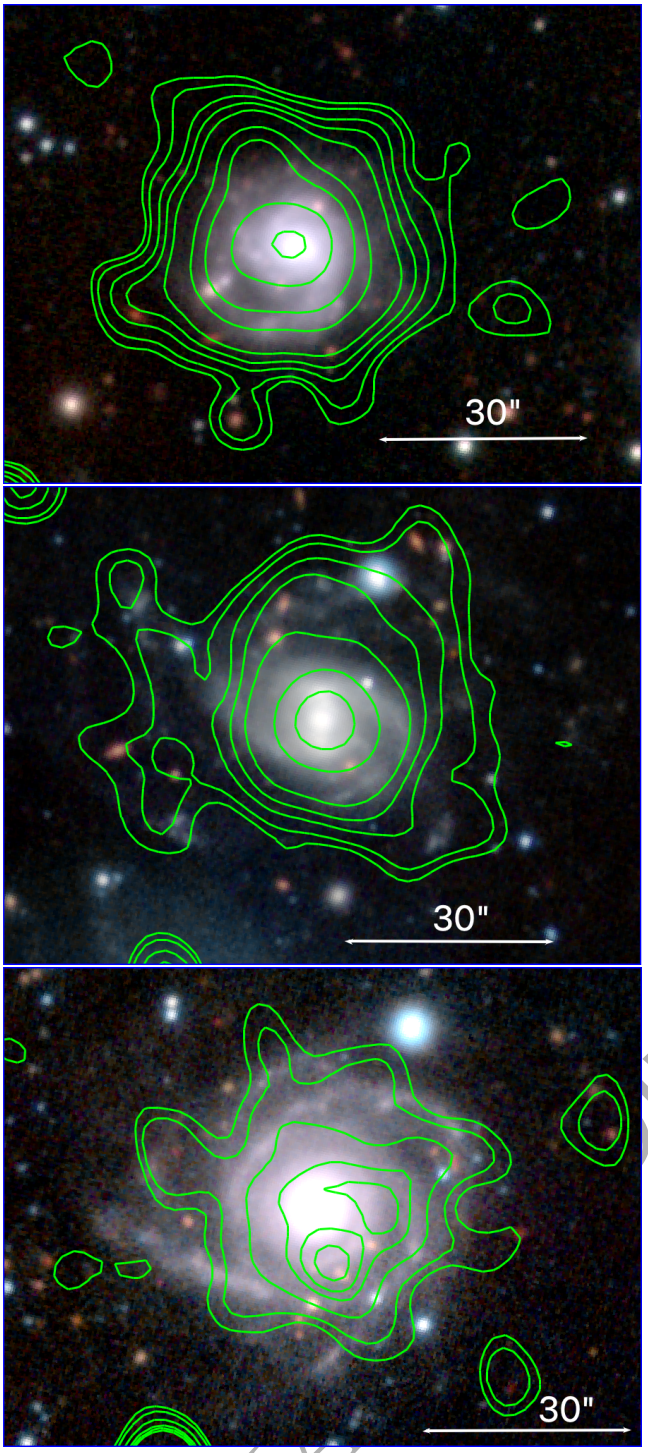

Figure 27. MeerKAT images of three nearby spiral galaxies: 2MASX J01215707–7516248 (top; a.k.a. Stribog), ESO 029–G047 (middle; a.k.a. Simargl) and ESO 029–G049 (bottom; a.k.a. Dažbog). MeerKAT (green) contours are 20, 30, 50, 70, 100, 200, 300, 500, 700 and 1000 μJy beam^{-1}. The background RGB image is from the VMC survey where R=Ks, G=J and B=Y band. Note that several radio point sources (some overlapping with the nearby galaxy) are clearly identified with much more distant AGN or radio galaxies.

Güdel M., 2002, ARA&A, 40, 217
Gvaramadze V. V., Kniazev A. Y., Oskinova L. M., 2019, MNRAS, 485, L6
Haberl F., Filipović M. D., Pietsch W., Kahabka P., 2000, A&AS, 142, 41
Haberl F., Sturm R., Filipović M. D., Pietsch W., Crawford E. J., 2012a, A&A, 537, L1
Haberl F., et al., 2012b, A&A, 545, A128
Hales C. A., Murphy T., Curran J. R., Middelberg E., Gaensler B. M., Norris R. P., 2012, MNRAS, 425, 979
Hancock P. J., Murphy T., Gaensler B. M., Hopkins A., Curran J. R., 2012, MNRAS, 422, 1812
Hancock P. J., Trott C. M., Hurley-Walker N., 2018, PASA, 35, e011
Haynes R. F., Klein U., Wielebinski R., Murray J. D., 1986, A&A, 159, 22
Henize K. G., 1956, ApJS, 2, 315
Heywood I., et al., 2022, ApJ, 925, 165
Hughes A., Staveley-Smith L., Kim S., Wolleben M., Filipović M., 2007, MNRAS, 382, 543
Hurley-Walker N., et al., 2019a, Publ. Astron. Soc. Australia, 36, e045
Hurley-Walker N., et al., 2019b, Publ. Astron. Soc. Australia, 36, e048
Inoue H., Koyama K., Tanaka Y., 1983, in Danziger J., Gorenstein P., eds, IAU Symposium Vol. 101, Supernova Remnants and their X-ray Emission. pp 535–540
Jacoby G. H., 1980, ApJS, 42, 1
Jankowski F., van Straten W., Keane E. F., Bailes M., Barr E. D., Johnston S., Kerr M., 2018, MNRAS, 473, 4436
Johnston S., et al., 2020, MNRAS, 493, 3608
Jonas J., 2016, "". SARAO, doi:10.22323/1.277.0001
Joseph T. D., et al., 2019, MNRAS, 490, 1202
Kaspi V. M., Johnston S., Bell J. F., Manchester R. N., Bailes M., Bessell M., Lyne A. G., D'Amico N., 1994, ApJ, 423, L43
Kavanagh P. J., et al., 2019, A&A, 621, A138
Knowles K., et al., 2022, A&A, 657, A56
Kwok S., 2005, Journal of Korean Astronomical Society, 38, 271
Kwok S., 2015, Highlights of Astronomy, 16, 623
Lamb R. C., Fox D. W., Macomb D. J., Prince T. A., 2002, ApJ, 574, L29
Leverenz H., Filipović M. D., Bojičić I. S., Crawford E. J., Collier J. D., Grieve K., Drašković D., Reid W. A., 2016, Ap&SS, 361, 108
Lindsay E. M., 1961, AJ, 66, 169
Luken K. J., et al., 2020, MNRAS, 492, 2606
Lyne A. G., et al., 1998, MNRAS, 295, 743
Maggi P., et al., 2016, A&A, 585, A162
Maggi P., et al., 2019, A&A, 631, A127
Maitra C., Ballet J., Filipović M. D., Haberl F., Tiengo A., Grieve K., Roper Q., 2015, A&A, 584, A41
Maitra C., Esposito P., Tiengo A., Ballet J., Haberl F., Dai S., Filipović M. D., Pilia M., 2021, MNRAS, 507, L1
Manchester R. N., Hobbs G. B., Teoh A., Hobbs M., 2005, AJ, 129, 1993
Manchester R. N., Fan G., Lyne A. G., Kaspi V. M., Crawford F., 2006, ApJ, 649, 235
Marocco F., et al., 2021, ApJS, 253, 8
Mauch T., Murphy T., Buttery H. J., Curran J., Hunstead R. W., Piestrzynski B., Robertson J. G., Sadler E. M., 2003, MNRAS, 342, 1117
Mauch T., et al., 2020, ApJ, 888, 61
McConnell D., McCulloch P. M., Hamilton P. A., Ables J. G., Hall P. J., Jacka C. E., Hunt A. J., 1991, MNRAS, 249, 654
McGee R. X., Newton L. M., Butler P. W., 1976, Australian Journal of Physics, 29, 329
Meixner M., et al., 2006, AJ, 132, 2268
Meixner M., et al., 2013, AJ, 146, 62
Meyssonnier N., Azzopardi M., 1993, A&AS, 102, 451
Morgan D. H., 1995, A&AS, 112, 445
Morgan D. H., Good A. R., 1985, MNRAS, 213, 491
Murphy T., et al., 2017, Publ. Astron. Soc. Australia, 34, e020
Noordam J. E., 2004, in Oschmann Jacobus M. J., ed., Society of Photo-Optical Instrumentation Engineers (SPIE) Conference Series Vol. 5489, Ground-based Telescopes. pp 817–825, doi:10.1117/12.544262
Norris R. P., et al., 2021, PASA, 38, e046
Oliveira J. M., et al., 2013, MNRAS, 428, 3001
Owen R. A., et al., 2011, A&A, 530, A132

Pavlović M. Z., Urošević D., Arbutina B., Orlando S., Maxted N., Filipović M. D., 2018, ApJ, 852, 84
Payne J. L., Filipović M. D., Reid W., Jones P. A., Staveley-Smith L., White G. L., 2004, MNRAS, 355, 44
Payne J. L., White G. L., Filipović M. D., Pannuti T. G., 2007, MNRAS, 376, 1793
Payne J. L., Filipović M. D., Crawford E. J., de Horta A. Y., White G. L., Stootman F. H., 2008, Serbian Astronomical Journal, 176, 65
Pedregosa F., et al., 2011, Journal of Machine Learning Research, 12, 2825
Pellegrini E. W., Oey M. S., Winkler P. F., Points S. D., Smith R. C., Jaskot A. E., Zastrow J., 2012, ApJ, 755, 40
Pennock C. M., et al., 2021, MNRAS, 506, 3540
Perley R. A., 1999, in Taylor G. B., Carilli C. L., Perley R. A., eds, Astronomical Society of the Pacific Conference Series Vol. 180, Synthesis Imaging in Radio Astronomy II. pp 383–+
Pietrzyński G., et al., 2019, Nature, 567, 200
Read A. M., Filipović M. D., Pietsch W., Jones P. A., 2001, A&A, 369, 467
Reid W. A., Payne J. L., Filipović M. D., Danforth C. W., Jones P. A., White G. L., Staveley-Smith L., 2006, MNRAS, 367, 1379
Reynolds J. E., 1994, ATNF Memo, AT/39.3/040
Reynolds S. P., Gaensler B. M., Bocchino F., 2012, Space Science Reviews, 166, 231
Roper Q., McEntaffer R. L., DeRoo C., Filipović M., Wong G. F., Crawford E. J., 2015, ApJ, 803, 106
Sanduleak N., MacConnell D. J., Philip A. G. D., 1978, PASP, 90, 621
Sano H., et al., 2017, ApJ, 843, 61
Sault R. J., Teuben P. J., Wright M. C. H., 1995, in Shaw R. A., Payne H. E., Hayes J. J. E., eds, Astronomical Society of the Pacific Conference Series Vol. 77, Astronomical Data Analysis Software and Systems IV. p. 433 (arXiv:astro-ph/0612759)
Smirnov O. M., 2011, A&A, 527, A106
Smirnov O. M., Tasse C., 2015, MNRAS, 449, 2668
Stanimirovic S., Staveley-Smith L., Dickey J. M., Sault R. J., Snowden S. L., 1999, MNRAS, 302, 417
Sturm R., et al., 2013a, A&A, 558, A3
Sturm R., et al., 2013b, A&A, 558, A101
Taylor M. B., 2005, in Shopbell P., Britton M., Ebert R., eds, Astronomical Society of the Pacific Conference Series Vol. 347, Astronomical Data Analysis Software and Systems XIV. p. 29
Titus N., et al., 2019, MNRAS, 487, 4332
Treumann R. A., 2006, A&ARv, 13, 229
Turtle A. J., Ye T., Amy S. W., Nicholls J., 1998, Publ. Astron. Soc. Australia, 15, 280
Vardoulaki E., et al., 2019, A&A, 627, A142
Virtanen P., et al., 2020, Nature Methods, 17, 261
Webb N. A., et al., 2020, A&A, 641, A136
Wenger M., et al., 2000, A&AS, 143, 9
White S. M., Franciosini E., 1995, ApJ, 444, 342
Whiting M., Humphreys B., 2012, Publ. Astron. Soc. Australia, 29, 371
Winkler P. F., Smith R. C., Points S. D., MCELS Team 2015, in Points S., Kunder A., eds, Astronomical Society of the Pacific Conference Series Vol. 491, Fifty Years of Wide Field Studies in the Southern Hemisphere: Resolved Stellar Populations of the Galactic Bulge and Magellanic Clouds. p. 343
Wong G. F., Filipović M. D., Crawford E. J., de Horta A. Y., Galvin T., Draskovic D., Payne J. L., 2011a, Serbian Astronomical Journal, 182, 43
Wong G. F., et al., 2011b, Serbian Astronomical Journal, 183, 103
Wong G. F., et al., 2012a, Serbian Astronomical Journal, 184, 93
Wong G. F., Filipović M. D., Crawford E. J., Tothill N. F. H., De Horta A. Y., Galvin T. J., 2012b, Serbian Astronomical Journal, 185, 53
Wright A., Otrupcek R., 1990, in PKS Catalog (1990).
Yamane Y., et al., 2021, ApJ, 918, 36
Yew M., et al., 2021, MNRAS, 500, 2336
Yu B., Zijlstra A., Jiang B., 2021, Universe, 7, 119
de Villiers M. S., Cotton W. D., 2022, AJ, 163, 135

SUPPORTING INFORMATION

Supplementary data are available at *MNRAS* online.

Table 4. Example of the point source catalogue of 108,330 objects in the directions of the SMC with its positions, integrated flux densities with associated uncertainty and spectral index.

Table 5. Example for the compact extended source list (total of 517 sources) at 1283.8 MHz derived from MeerKAT survey.

Please note: Oxford University Press is not responsible for the content or functionality of any supporting materials supplied by the authors. Any queries (other than missing material) should be directed to the corresponding author for the article.